JOURNAL of the MEXICAN CHEMICAL SOCIETY

https://www.jmcs.org.mx/

Article

Open Access

J. Mex. Chem. Soc. **2026**, *70(1):e2498*

Received June 5th, 2025
Accepted February 9th, 2026

http://dx.doi.org/10.29356/jmcs.v70i1.2498
e-location ID: 2498

Keywords:
DFT, CDFT, HDS, 4,6-DMDBT, MoS_2 catalyst

Palabras clave:
DFT, CDFT, HDS, 4,6-DMDBT, Catalizador de MoS_2

***Corresponding author:**
Héctor Martínez-Grimaldo
email: hectorgrimaldo@quimica.unam.mx

ISSN-e 2594-0317

Relationships of Structural, Electronic and Energy Properties of Free and Adsorbed Molecules Over MoS_2 Model Clusters, Involved in the DDS and HYDS Pathways for the HDS Of 4,6-DMDBT. A CDFT Study

Héctor Martínez-Grimaldo[1]*, Alan Miralrio[2], Perla Castillo-Villalón[1], Miguel Castro[3], Jorge Ramírez[1]

[1]UNICAT, Departamento de Ingeniería Química, Facultad de Química, UNAM, Ciudad Universitaria, Coyoacán, Ciudad de México 04510, México.
[2]Tecnológico de Monterrey, Escuela de Ingeniería y Ciencias, Ave. Eugenio Garza Sada 2501, Monterrey 64849, NL, México.
[3]Departamento de Física y Química Teórica, Facultad de Química, UNAM, Ciudad Universitaria, Coyoacán, Ciudad de México 04510, México.

Abstract. The reaction pathways, direct desulfurization (DDS) and hydrogenation-desulfurization (HYDS), in the HDS of 4,6-DMDBT on MoS_2 clusters representing different models of coordinatively unsaturated sites (CUS) and brim active sites are analyzed using Density Functional Theory (DFT) and related concepts (CDFT). Reactivity indices of free molecule are related to the structural and energy properties of the chemisorbed molecules in model clusters. The results show that the bond lengths between the S atom of the adsorbed organic molecules and the Mo atom at CUS are multilinearly related to nucleophilic indices of nucleophilic centers of free molecules. In the DDS pathway, the high adsorption energy and the large S-Mo bond length of 3,3'-dimethyl-biphenyl-2-thiol suggest that the controlling reaction step is the hydrogenolysis of its S-C bond. It was found that a multilinear relationship exists between surface reaction energies (hydrogenation, hydrogen transfer, and hydrogenolysis) and reaction energies calculated for free molecules, electrophilicity global indices, and HOMO-LUMO gaps of free sulfur-containing molecules. Similarly,

J. Mex. Chem. Soc. **2026**, *70(1):e2498*
Regular Issue

ISSN-e 2594-0317

multilinear relationships were found between adsorption energies of the molecules on CUS and brim sites of model clusters and the nucleophilic indices of the different nucleophilic centers in free molecule.

Resumen. Se analizan las rutas de reacción, desulfuración directa (DDS) e hidrogenación-desulfuración (HYDS), en la HDS de 4,6-DMDBT en cúmulos modelos de MoS_2 que representan diferentes sitios coordinativamente insaturados (CUS) y sitios activos *brim* mediante la Teoría del Funcional de la Densidad (DFT) y los conceptos relacionados (CDFT). Los índices de reactividad de moléculas libres son relacionados con las propiedades estructurales y de energía de las moléculas quimisorbidas en los cúmulos modelo. Los resultados muestran que las longitudes de enlace entre el átomo de S de las moléculas orgánicas adsorbidas y el átomo de Mo en un CUS están relacionadas multilinealmente con los índices nucleofílicos de los centros nucleofílicos de las moléculas libres. En la ruta DDS, la alta energía de adsorción y la gran longitud de enlace S-Mo del 3,3'-dimetil-bifenil-2-tiol sugieren que el paso de reacción controlante es la hidrogenólisis de su enlace S-C. Se encontró una relación multilínea entre las energías de reacción superficial (hidrogenación, transferencia de hidrógeno e hidrogenólisis) y las energías de reacción calculadas para moléculas libres, los índices globales de electrofilicidad y las brechas HOMO-LUMO de las moléculas libres que contienen azufre. De igual manera, se encontraron relaciones multilíneas entre las energías de adsorción de las moléculas en los sitios *brim* y CUS de los cúmulos modelo y los índices nucleofílicos de los diferentes centros nucleofílicos en las moléculas libres.

Introduction

Hydrodesulfurization (HDS) is the most important process to remove sulfur and produce ultraclean fuels from petroleum. Conventional HDS catalysts are based on MoS_2, promoted with Co (CoMoS) or Ni (NiMoS) and supported on γ-Al_2O_3 [1,2]. Two main pathways are reported in the literature for the HDS reaction over conventional catalysts, the direct desulfurization (DDS) and hydrogenation-desulfurization (HYDS) [2]. Fig. 1 shows the key reaction steps of the pathways for 4,6-DMDBT. According to STM studies and Topsøe's model [3,4], the DDS pathway proceeds on coordinatively unsaturated sites (CUS), whereas the HYDS pathway proceeds on brim sites.

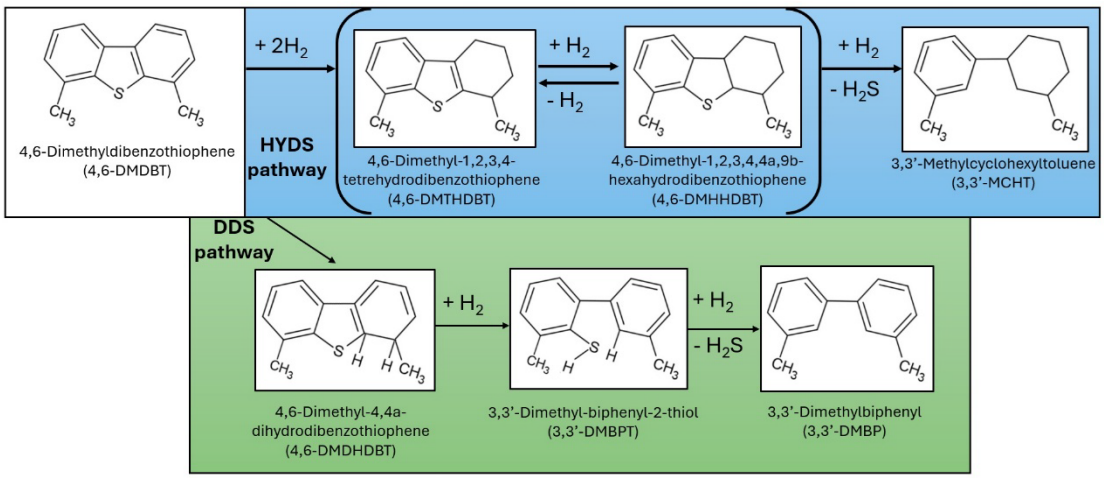

Fig. 1. Schemes of the DDS and HYDS pathways of 4,6-DMDBT, adapted from [5].

Improvement and understanding of HDS catalysts require deep knowledge about the reactivity and the molecular interactions of reactants, intermediates, and products with the active sites. To improve the

http://dx.doi.org/10.29356/jmcs.v70i1.2498

J. Mex. Chem. Soc. **2026**, *70(1):e2498*
Regular Issue

ISSN-e 2594-0317

HDS catalysts, two approaches have been used, namely the experimental approach and theoretical approach based on first principles. In the first, different additives, supports, and preparation conditions have been proposed to enhance the promotion and dispersion of the active phases [6–12]. In the second approach, the most used models are those based on Density Functional Theory (DFT), which have made it possible to understand the structure of the catalysts, the adsorption of reactive molecules and the determination of reaction steps [13–19].

Another theoretical approach used to study the reactivity and selectivity for chemical reactions is the Conceptual Density Functional Theory (CDFT) [20,21]. The CDFT uses several reactivity indices (e.g., electronic chemical potential, chemical hardness, electrophilicity, condensed Fukui functions) to describe chemical behavior and to identify the most electrophilic and nucleophilic regioselectivity centers, and the most probable regions where free radical attacks occur. Some reactivity indices, like global electrophilicity and hardness, can be related to reaction energies, activation energy, or logarithm of kinetic constant. The global electrophilicity index of reactants is widely used and shows a linear relationship with reaction energies [22], activation energies for several reactions [23,24], and the logarithm of the kinetic constant [25].

The CDFT has been used to describe the reactivity of sulfur-containing molecules in the HDS process [26–28]. Li and coworkers [28] correlated the experimental HDS selectivity in CoMoS and NiMoS catalysts with the hardness index of free molecules (4,6-DMDBT, 4-MDBT, DBT and BT (benzothiophene)), without considering interactions with the catalyst. They concluded that the compounds exhibiting high selectivity towards DDS have a high value of hardness index. These authors proposed that ionization energy, hardness, and S-C bond length of the reactive molecules are good descriptors of activity and selectivity of the catalytic HDS reaction. García-Cruz and coworkers [27] found that the proton affinity and HOMO energy of a series of free sulfur-containing molecules show linear relationship with the total pseudo-first-order rate constant of HDS. The reactivity indices in the above-mentioned reports were related to the overall reactivity of the HDS reaction, but the DDS and HYDS pathways were not considered separately. In general, there is a lack of reports that use CDFT to carry out reactivity analysis following the reaction trajectory of reactants, intermediates, and reaction products for both DDS and HYDS pathways, as well as the interactions of the involved molecules with the active sites. Therefore, the understanding of the HDS reaction network is not complete, and some important features, such as the determination of the rate-limiting steps in the reaction pathways, are still missing.

In this work, a new simple methodology is proposed to identify the rate-limiting step for each reaction pathway of the HDS of 4,6-DMDBT. The methodology analyzes the reactivity of 4,6-DMDBT, intermediates, and reaction products for both DDS (4,6-DMDHDBT, 3,3'-DMBPT, and 3,3'-DMBP) and HYDS (4,6-DMTHDBT, 4,6-DMHHDBT, and 3,3'-MCHT), as shown in Fig. 1, using DFT and CDFT. The study of the reactivity of intermediates will provide further information about the reaction energies of each step, which will help identify the elementary steps that are the most thermodynamically stable for both reaction pathways. This methodology is based on the possible existence of multilinear relationships between electronic and structural properties of free and adsorbed molecules involved in both pathways, as well as reaction energies, with and without molecule-catalyst interactions. These multilinear relationships can provide rapid approximations at low computational costs. For the analysis, the following structural and electronic properties of free and adsorbed molecules are considered: S-C bond lengths of both ring types (hydrogenated and non-hydrogenated aromatic rings), HOMO-LUMO gaps, global electrophilicity index, and condensed nucleophilicity index.

To calculate the properties of the adsorbed molecules, three model clusters were proposed to represent active sites: 1) $Mo_{12}S_{25}$-MoE-33 for hydrogen activation site on Mo-edges, 2) $Mo_{12}S_{23}$-MoE-0 for CUS, and 3) $Mo_{12}S_{24}$-SE-50 for brim sites and hydrogen activation sites on S-edges. In addition, two adsorption modes for sulfur-containing molecules were considered: 1) σ-perpendicular adsorption mode at CUS, and 2) π-planar adsorption mode at brim active sites. The relevant structural (e.g., bond lengths between S atom of sulfur-containing molecules and Mo atom of the $Mo_{12}S_{23}$-MoE-0 cluster, and distance between aromatic rings and basal plane of the $Mo_{12}S_{24}$-SE-50 cluster) and electronic (such as HOMO, LUMO, and band gaps, and global reactivity indices) properties are calculated.

There are three main nucleophilic centers for the species involved in the HDS of 4,6-DMDBT: the S atom, the hydrogenated aromatic ring, and the non-hydrogenated aromatic ring. On these grounds, the

http://dx.doi.org/10.29356/jmcs.v70i1.2498

J. Mex. Chem. Soc. **2026**, *70(1):e2498*
Regular Issue

ISSN-e 2594-0317

condensed philicity indices of nucleophilic centers in free molecules can be associated with the structural properties of adsorbed molecules and their adsorption energies. Multilinear relationships can be constructed by considering each of the contributions of nucleophilic centers together with properties related to adsorption. This approach has not yet been applied to the study of the HDS reactions. Furthermore, the existence of a multilinear relationship between surface reaction energies (hydrogenation, hydrogenolysis and hydrogen transfer reactions) and the reaction energies without molecule-catalyst interaction is explored, as well as the HOMO-LUMO gaps and the electrophilicity index of free molecules. Finally, it is possible that there are relationships between the energy corrections of free and adsorbed molecules, which may allow a rapid estimation of these properties, reducing the high computation cost associated with calculation of vibrational frequencies of adsorbed molecules.

Computational methods

Density Functional Theory calculations

The Density Functional Theory (DFT) calculations were performed using a spin unrestricted open-shell approach and the model cluster with the Gaussian 09 package, Revision D.01 [29], at the UPBE-GGA/DEF2TZVP level of theory [30–35]. The empirical dispersion correction of Grimme GD3(BJ) [36] was employed to include van der Waals interactions, which are involved in the adsorption of molecules on the model clusters. Vibrational frequency calculations of free molecules, adsorbed molecules, and model clusters were carried out using analytical and numerical differentiation methods. The PBE-GGA exchange-correlation functional, including empirical dispersion corrections, has been employed to study various catalyst systems for HDS [37–40]. The vibrational frequency calculations were validated for all structures to avoid any imaginary frequencies. Atomic partial charges were determined by Hirshfeld population analysis (HPA) [41]. HPA was selected because a previous comparison with Mulliken population analysis (MPA) demonstrated that HPA provides a charge distribution more consistent with the localization of active sites at catalyst edges. According to [42], HPA exhibits a lower dependence on the basis set than MPA, which allows the partial charges of Mo atoms to be represented with *d* orbitals. The zero-point energies (ZPE), internal thermal correction energies (E_{corr}), thermal correction to enthalpies (H_{corr}), thermal correction to Gibbs energies (G_{corr}) and Gibbs energies under HDS conditions (593.15 K and 86 atm) were estimated with the partition function method [43] using the thermochemistry library of Gaussian 09 package. After the optimization of the proposed structures, ionization potential, affinity energy, bond lengths, bond angles from our results and those reported by other authors for several free molecules involved in the industrial HDS processes (dibenzothiophene or DBT, cyclohexylbenzene or CHB, bicyclohexyl or BCH, biphenyl or BP, 4,6-DMDBT, naphthalene, tetralin, decalin, H_2S, and H_2) were compared to validate the level of theory.

Reactivity analysis and CDFT calculations

The chemical reactivity of free molecules, model clusters, and adsorbed molecules was analyzed through the calculation of HOMO-LUMO gaps ($\varepsilon_{HOMO-LUMO}$), S-C bond length, and global and local condensed reactivity indices. For free molecules, reactivity indices were evaluated for reagents, intermediates, and products of the DDS and HYDS reaction pathways, following the schemes presented in Fig. 1. The global electrophilicity index (ω) was obtained from the electronic chemical potential (μ) and chemical hardness (η) indices using the following equation:

$$\omega = \frac{\mu^2}{2\eta} \tag{1}$$

The equations used to calculate the μ and η indices are provided in Section S1 of the Supporting Information (SI). The ω index is a measure of the electrophilic capacity of a chemical species to acquire

J. Mex. Chem. Soc. **2026**, *70(1):e2498*
Regular Issue

ISSN-e 2594-0317

electron density, given by μ, and its resistance to electron density exchange with the environment, given by η. Strong electrophiles exhibit high ω values, whereas strong nucleophiles exhibit low ω values [20,21].

To compare the ability of atoms in different molecules to donate or accept electrons, the condensed philicity indices of atom α for electrophilic (ω_α^-), nucleophilic (ω_α^+), and radical (ω_α^0) attacks are calculated as follows:

$$\omega_\alpha^- = \omega f_\alpha^- \tag{2}$$

$$\omega_\alpha^+ = \omega f_\alpha^+ \tag{3}$$

$$\omega_\alpha^0 = \omega f^0 \tag{4}$$

where f_α^-, f_α^+ and f_α^0 are the condensed Fukui functions associated with electrophilic, nucleophilic, and radical attacks. Details regarding the calculation of the Fukui functions are presented in Section S1 of the SI. A high value of ω_α^-, ω_α^+, and ω_α^0 implies that atom α exhibits strong nucleophilic and electrophilic character, and a pronounced tendency to accept free radicals [20,21].

Reaction steps of the DDS and HYDS pathways in the HDS of 4,6-DMDBT

Based on the DDS and HYDS pathways shown in Fig. 1, the reaction mechanism presented in Table 1 was derived , where σ_{Mo} and σ_S denote the S atoms at which an S-H group forms on the Mo-edge and S-edge, respectively, α and β refer to a CUS and brim active site. In addition to the steps shown in Fig. 1 for the HYDS pathway, it is proposed that the 4,6-DMTHDBT and 4,6-DMHHDBT molecules are desorbed from the brim sites, and subsequently adsorbed on a CUS to form 3,3'-MCHT, because these species have been reported experimentally [44]. Additionally, to understand the DDS pathway, it is considered that 4,6-DMDHDBT and 3,3'-DMBPT formation as reaction steps, even though they are not observed experimentally, since they are unstable intermediates that are formed by the molecule-active site interaction. The desorption of 3,3'-DMBP (DDS pathway) and 3,3'-MCHT (HYDS pathway) products is not considered in Table 1. This is because the S atoms involved in breaking the S-C bonds of the 3,3-DMBPT and 4,6-DMHHDBT molecules remain attached to the CUS as adsorbed H_2S, while 3,3'-DMBP and 3,3-MCHT molecules are released during the hydrogenolysis step (see reaction 5 of the DDS pathway and reaction 10 of the HYDS pathway in Table 1). The hydrogenolysis reactions are considered as the addition of hydrogen atoms to S and C atoms bonded within the sulfur-containing molecule, accompanied by the simultaneous cleavage of the S-C bond.

Table 1. Reaction steps of the DDS and HYDS pathways in the HDS of 4,6-DMDBT[a].

DDS pathway	
1) Hydrogen activation on two σ_{Mo} sites.	$H_2 + 2\sigma_{Mo} \rightleftarrows 2H{\cdot}\sigma_{Mo}$
2) Adsorption of 4,6-DMDBT on an α site.	4,6-DMDBT + α ⇄ 4,6-DMDBT· α
3) Hydrogenation of 4,6-DMDBT on an α site.	4,6-DMDBT· α + $2H{\cdot}\sigma_{Mo}$ ⇄ 4,6-DMDHDBT·α + $2\sigma_{Mo}$
4) Hydrogen transfer on an α site.	4,6-DMDHDBT·α ⇄ 3,3'-DMBPT· α
5) Hydrogenolysis of 3,3'-DMBPT on an α site.	3,3'-DMBPT·α + $2H{\cdot}\sigma_{Mo}$ ⇄ 3,3'-DMBP + $H_2S{\cdot}\alpha$ + $H{\cdot}\sigma_{Mo}$
6) Desorption of H_2S from an α site.	$H_2S{\cdot}\alpha \rightleftarrows H_2S + \alpha$

http://dx.doi.org/10.29356/jmcs.v70i1.2498

J. Mex. Chem. Soc. **2026**, *70(1):e2498*
Regular Issue

ISSN-e 2594-0317

HYDS pathway	
1) Hydrogen activation on two σ_S sites.	$H_2 + 2\sigma_S \rightleftarrows 2H{\cdot}\sigma_S$
2) Adsorption of 4,6-DMDBT on a β site.	4,6-DMDBT + β ⇄ 4,6-DMDBT· β
3) Hydrogenation of 4,6-DMDBT on a β site.	4,6-DMDBT· β + $4H{\cdot}\sigma_S \rightleftarrows$ 4,6-DMTHDBT· β + $4\sigma_S$
4) Hydrogenation of 4,6-DMTHDBT on a β site.	4,6-DMTHDBT·β + $2H{\cdot}\sigma_S \rightleftarrows$ 4,6-DMHHDBT·β + $2\sigma_S$
5) Desorption of 4,6-DMTHDBT from a β site.	4,6-DMTHDBT·β ⇄ 4,6-DMTHDBT + β
6) Desorption of 4,6-DMHHDBT from a β site.	4,6-DMHHDBT·β ⇄ 4,6-DMHHDBT + β
7) Adsorption of 4,6-DMTHDBT on an α site.	4,6-DMTHDBT + α ⇄ 4,6-DMTHDBT·α
8) Adsorption of 4,6-DMHHDBT on an α site.	4,6-DMHHDBT + α ⇄ 4,6-DMHHDBT·α
9) Hydrogenation of 4,6-DMTHDBT on a α site.	4,6-DMTHDBT·α + $2H{\cdot}\sigma_{Mo} \rightleftarrows$ 4,6-DMHHDBT·α + $2\sigma_{Mo}$
10) Hydrogenolysis of 4,6-DMHHDBT on a α site.	4,6-DMHHDBT·α + $4H{\cdot}\sigma_{Mo} \rightleftarrows$ 3,3'-MCHT + $H_2S{\cdot}\alpha + 2\sigma_{Mo}$

[a] σ_{Mo} is a S atom on a Mo-edge, σ_S is a S atom on a S-edge, α is a CUS and β is a brim active site.

The reaction energies (ΔE_0) of the steps in Table 1 were calculated and corrected to HDS conditions (593.15 K and 86 atm) to estimate reaction enthalpy (ΔH_R), Gibbs energy (ΔG_R), and equilibrium constant (K_{eq}) for each reaction step. The reaction energies and equilibrium constants were calculated using the following equations:

$$\Delta E_0 = \sum_{Products} \nu_j E_0 - \sum_{Reagents} \nu_j E_0 \tag{5}$$

$$K_{eq} = \exp(-\Delta G_R / RT) \tag{6}$$

where ν_j is a suitable stoichiometric coefficient according to the reaction steps presented in Table 1. Equations such as (5) are used to calculate ΔH_R and ΔG_R. The subscript "ad" denotes adsorption, while the subscripts H2 and H2S denote H2 dissociation and H2S chemisorption, respectively.

The surface reactions (hydrogenation, hydrogen transfer, and hydrogenolysis steps) are presented in Table 1. The ΔE_0, ΔH_R, ΔG_R and K_{eq} of the surface reactions were calculated for reaction without and with molecule-catalyst interaction. Reaction energies without molecule- catalyst interactions were obtained from the total energies of free molecules, whereas reaction energies with molecule-cluster interaction were estimated using the total energies of adsorbed molecules. This comparison was made to analyze possible relationships between the reaction energies of catalytic steps and those of the same steps without molecule-cluster interaction.

The adsorption free energies of H2 ($(\Delta G_{ad})_{H_2}$) and H2S ($(\Delta G_{ad})_{H_2S}$) must be corrected to account for the presence of H2 and H2S in the reaction environment [15, 45]. The corrected free energy for H2 partial pressure, $(\Delta G_{ad})_{H_2 corr}$, is estimated using the following equation:

$$(\Delta G_{ad})_{H_2 corr} = (\Delta G_{ad})_{H_2} + RT \ln(p_{H_2}^{-1}) \tag{7}$$

The adsorption free energy corrected for H2S partial pressure, $(\Delta G_{ad})_{H_2 S corr}$, is obtained from the following equation:

$$(\Delta G_{ad})_{H_2 S corr} = (\Delta G_{ad})_{H_2 S} + RT \ln(p_{H_2 S}^{-1}) \tag{8}$$

J. Mex. Chem. Soc. **2026**, *70(1):e2498*
Regular Issue

ISSN-e 2594-0317

Relevant HDS conditions are 573-700 K, 1-200 bar of H2 partial pressure, and 10^{-4}-10^{-1} p_{H_2S}/p_{H_2} ratio [14]. Highly reductive conditions (60 bar H2, 10^{-6} bar H2S) were considered in the calculation of $(\Delta G_{ad})_{H_2 corr}$ and $(\Delta G_{ad})_{H_2 S corr}$.

Model clusters and adsorption modes

Under HDS conditions, MoS_2 catalysts particles acquire a deformed hexagonal shape, with the S-edges $(\bar{1}010)$ being slightly shorter than the Mo-edge $(10\bar{1}0)$ [46] (approximately five Mo atoms for the S-edge and six Mo atoms for the Mo-edge). At low reaction times or under high H_2 pressures, the HDS process can be regarded as occurring under highly reducing conditions (low p_{H_2S}/p_{H_2} ratio). In this case the Mo-edge may exhibit S coverages below 50 % (two S atoms per Mo) and H coverages below 33 % (one H atom per Mo atom). The S-edge may exhibit S and H coverages exceeding 50 % and 67 %, respectively [14,15]. Accordingly, the MoS_2 catalyst under HDS reducing conditions may adopt the shape shown in Fig. 2**(a)**. The positions of the proposed model clusters ($Mo_{12}S_{23}$-MoE-0, $Mo_{12}S_{25}$-MoE-33, and $Mo_{12}S_{24}$-SE-50) within the catalyst crystal are illustrated in Fig. 2**(b)**-2**(d)**. The model clusters were developed using GaussView 5.0.8 software and crystallographic data from Crystallography Open Database [47]. The edge coverage of the model clusters proposed in this study is consistent with the presence of 50 % S coverage at the S-edge and less than 50 % at Mo-edge under highly reductive conditions, such as those present under HDS reaction conditions [14,15].

The model cluster $Mo_{12}S_{23}$-MoE-0 (Fig. 2**(b)**) represents a fragment of the Mo-edge on the $(10\bar{1}0)$ plane with 0 % S coverage and contains CUS, where sulfur-containing molecules can adsorb. The CUS are low-coordination Mo surface atoms, formed by the removal of sulfur atoms from the edges under reducing conditions with hydrogen. The DDS pathway is mainly associated with CUS on Mo-edges [48,49]. The $Mo_{12}S_{25}$-MoE-33 model cluster (Fig. 2**(c)**) is a fragment of the Mo-edge adjacent to the $(10\bar{1}0)$ plane with 33 % S coverage and exhibits σ_{Mo} active sites, where hydrogen activation occurs. The 33 % S vacancy on the $(10\bar{1}0)$ plane of the $Mo_{12}S_{25}$-MoE-33 cluster was considered to better represent the position of the S atoms and S-H groups on the Mo-edge, in accordance with Rosen et al. [15]. The $Mo_{12}S_{23}$-MoE-0 and $Mo_{12}S_{25}$-MoE-33 model clusters are the smallest deformed hexagonal MoS_2 crystals, containing three Mo atoms on the Mo-edges and two Mo atoms on the S-edges. Both clusters exhibit 50 % S coverage on edges, except at the Mo-edge of $(10\bar{1}0)$ plane.

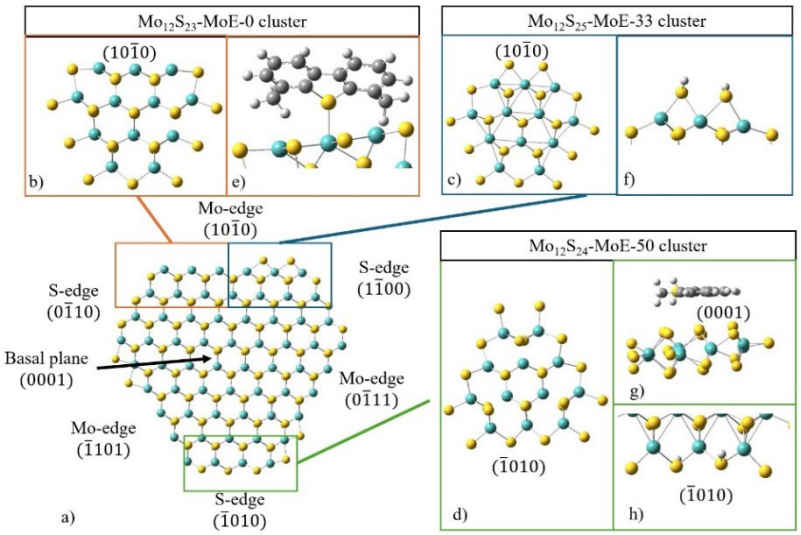

Fig. 2. Structure of MoS_2 catalysts under reducing HDS conditions and adsorption modes of molecules. Cyan, yellow, gray, and white balls represent Mo, S, C and H atoms, respectively. The model clusters employed in this work are highlighted with frames. **(a)** Localization of model clusters and adsorption modes in MoS_2 catalysts particles, **(b)** $Mo_{12}S_{23}$-MoE-0 model cluster, **(c)** $Mo_{12}S_{25}$-MoE-33 model cluster, **(d)** $Mo_{12}S_{24}$-SE-50 model cluster, **(e)** σ-perpendicular adsorption mode on CUS for 4,6-DMDBT, **(f)** S-H group formation in the Mo-edge, **(g)** π-planar adsorption mode on brim active sites for 4,6-DMDBT, and **(h)** S-H group formation in the S-edge.

http://dx.doi.org/10.29356/jmcs.v70i1.2498

J. Mex. Chem. Soc. **2026**, *70(1):e2498*
Regular Issue

ISSN-e 2594-0317

The $Mo_{12}S_{24}$-SE-50 model cluster (Fig. 2**(d)**) is a part of the S-edge on the $(\bar{1}010)$ plane of the MoS_2 catalyst crystal, with 50 % S coverage. It contains brim active sites located above the (0001) basal plane, as well as σ_S hydrogen-activation sites on $(\bar{1}010)$ plane. The brim sites are metallic zones located above the basal plane, which extend over the first three or four rows of atoms around the edges [48,49]. The $Mo_{12}S_{24}$-SE-50 model cluster is the smallest MoS_2 crystal containing three Mo atoms on the S-edges and two Mo atoms on the Mo-edges This deformed hexagonal cluster is intended to contain the molecular orbitals that constitute the brim sites (due to geometric similarity) while simultaneously reducing computational cost.

Different adsorption modes are proposed for H_2 and sulfur-containing molecules at σ_{Mo}, σ_S, CUS and brim active sites of the model clusters (Fig. 2). Hydrogen activation is assumed to occur via homolytic dissociation, involving the formation of two S-H groups on σ_{Mo} and σ_S sites in the $(10\bar{1}0)$ plane of the $Mo_{12}S_{25}$-MoE-33 model cluster (Fig. 2**(f)**) and in the $(\bar{1}010)$ plane of the $Mo_{12}S_{24}$-MoE-50 model cluster (Fig. 2**(h)**). The σ-perpendicular and π-planar adsorption modes proposed in this work are illustrated in Figs 2**(e)** and 2**(g)** and are consistent with those reported by other authors [50,51].

The σ-perpendicular adsorption mode is located on the unsaturated Mo atoms of the Mo-edge in the $(10\bar{1}0)$ plane of the $Mo_{12}S_{23}$-MoE-0 model cluster (Fig. 2**(e)**). This mode represents the chemisorption of the sulfur atom in 4,6-DMDBT, 4,6-DMDHDBT, 3,3'-DMBPT, 4,6-DMTHDBT and 4,6-DMHHDBT molecules at a CUS via σ-bond formation between the S atom of the sulfur-containing molecule and the Mo atom of the cluster. On the other hand, the π-planar adsorption mode occurs on the (0001) basal plane of the $Mo_{12}S_{24}$-SE-50 model cluster (Fig. 2**(g)**). This mode represents the physisorption of sulfur-containing molecules (4,6-DMDBT, 4,6-DMTHDBT, and 4,6-DMHHDBT) at brim active sites. This configuration arises from the interaction between the π-orbitals of the aromatic molecules and the brim active site.

Results and discussion

Structural and electronic properties of free molecules and model clusters

Validation of the theoretical level for free molecules and model clusters is presented in Section S2 of the SI, showing good agreement with experimental data. Bond-length errors for free molecules were ≤ 2 %, whereas the maximum absolute bond-lengths error in the MoS_2 clusters was 3.5 %, demonstrating that the theoretical level (UPBE-GGA/DEF2TZVP) reliably predicts the structures of molecules and clusters.

Structural formulas and optimized structures of the free molecules are illustrated in Fig. 3, including the numbering of the most relevant atoms. Table 2 summarizes the relevant structural (S1-C6 and S1-C13 bond lengths, according to Fig. 3) and electronic (HOMO-LUMO gap, global electrophilicity, and condensed nucleophilicity indices) properties of free molecules involved in the DDS and HYDS pathways of 4,6-DMDBT HDS. A detailed reactivity analysis of free molecules is provided in Section S3 of the SI.

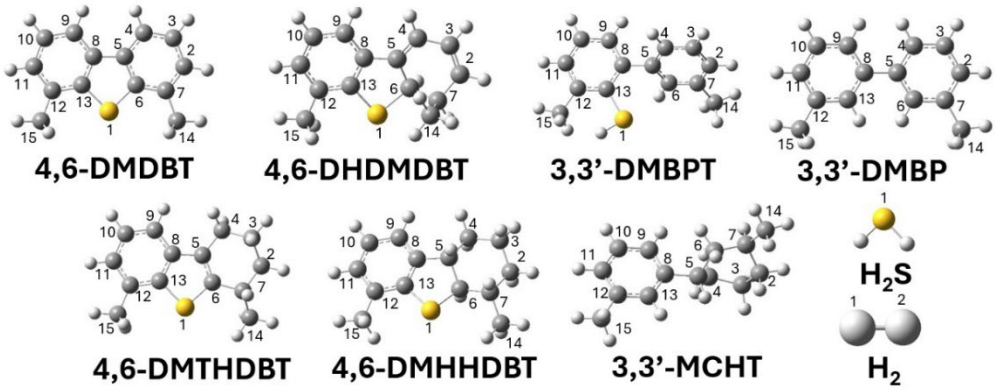

Fig. 3. Structural formulas of the free molecules.

http://dx.doi.org/10.29356/jmcs.v70i1.2498

J. Mex. Chem. Soc. **2026**, *70(1):e2498*
Regular Issue

ISSN-e 2594-0317

Table 2. Relevant structural and electronic properties of free molecules.

Molecule and clusters	Structural and electronic properties*						
	r_{S1-C6} (Å)	r_{S1-C13} (Å)	$\varepsilon_{HOMO-LUMO}$ (eV)	ω (eV)	ω_{S1}^{-} (eV)	ω_{A1}^{-} (eV)	ω_{A2}^{-} (eV)
4,6-DMDBT	1.75	1.75	3.40	1.69	0.33	0.40	0.40
4,6-DMDHDBT	1.84	1.76	2.27	1.94	0.32	0.47	0.43
3,3'-DMBPT	3.12	1.78	3.63	1.56	0.32	0.28	0.36
3,3'-DMBP			3.56	1.75		0.53	0.53
4,6-DMTHDBT	1.75	1.74	3.60	1.38	0.22	0.24	0.37
4,6-DMHHDBT	1.85	1.77	3.82	1.12	0.30	0.06	0.33
3,3'-MCHT			4.72	1.26		0.13	0.49
H_2			11.43	1.94			
H_2S			5.68	1.23	0.94		
$Mo_{12}S_{25}$-MoE-33			0.64(α)/0.31(β)	8.97			
$Mo_{12}S_{23}$-MoE-0			0.29	8.61			
$Mo_{12}S_{24}$-SE-50				10.92			

* r_{S1-C6} and r_{S1-C13} are the S1-C6 and S1-C13 bond lengths, respectively, and $\varepsilon_{HOMO-LUMO}$ is the band gap.

Reaction energies without molecule-catalyst interactions (ΔE_0, ΔH_R, ΔG_R and K_{eq}) at 593.15 K and 85 atm during the DDS and HYDS pathways are reported in Table 3. The overall equilibrium constant ($K_{eq} = 38.23$) of the DDS pathway indicates spontaneity of the total reaction. In contrast, all HYDS pathway steps, without molecule-cluster interaction, are spontaneous under HDS conditions, and the HYDS pathway ($K_{eq} = 1.68 \times 10^{10}$) is thermodynamically much more favorable than the DDS pathway.

Reaction energies without molecule-catalyst interaction reflect change due solely to molecular structure. Therefore, additional parameters of free molecules that are related to the ability of the molecules to hydrogenate ($\varepsilon_{HOMO-LUMMO}$) and interact with the active sites (ω) should be also considered when estimating catalytic reaction energies.

Table 3. Reaction energies and equilibrium constants of DDS and HYDS pathway reactions without molecule-catalyst interaction.

Reaction	ΔE_0 (eV)	ΔG_R (eV)*	ΔH_R (eV)	K_{eq}
DDS pathway				
4,6-DMDBT + H_2 ⇌ 4,6-DMDHDBT	0.47	1.05	0.76	1.23×10^{-9}
4,6-DMDHDBT + ⇌ 3,3'-DMBPT	-0.44	-0.71	-0.48	1.19×10^{6}
3,3'-DMBPT + H_2 ⇌ 3,3'-DMBP + H_2S	-0.50	-0.52	-0.50	2.62×10^{4}
TOTAL: 4,6-DMDBT + $2H_2$ ⇌ 3,3'-DMBP + H_2S	-0.47	-0.19	-0.22	38.23

http://dx.doi.org/10.29356/jmcs.v70i1.2498

J. Mex. Chem. Soc. **2026**, *70(1):e2498*
Regular Issue

ISSN-e 2594-0317

Reaction	ΔE_0 (eV)	ΔG_R (eV)*	ΔH_R (eV)	K_{eq}
HYDS pathway				
4,6-DMDBT + $2H_2$ ⇌ 4,6-DMTHDBT	-1.48	-0.25	-0.85	145.71
4,6-DMTHDBT + H_2 ⇌ 4,6-DMHHDBT	-0.68	-0.04	-0.38	2.36
4,6-DMHHDBT + H_2 ⇌ 3,3'-MCHT + H_2S	-0.80	-0.90	-0.38	4.74×10^7
TOTAL: 4,6-DMDBT + $5H_2$ ⇌ 3,3'-MCHT + H_2S	-2.96	-1.19	-1.61	1.63×10^{10}

*K_{eq}, ΔG_R and ΔH_R at 593.15 K and 85 atm

Fig. 4 show the optimized structures of MoS_2 model clusters, respectively. Table 4 reports the ω values for model clusters, and a more detailed analysis of their structural and electronic properties is provided in the Section S4 of the SI. The Molecular orbitals of the model clusters (Fig. S2) demonstrates that they adequately represent the catalytic active sites. On the other hand, the model clusters have higher ω values (e.g., 8.61 eV for $Mo_{12}S_{23}$-MoE-0, see Table 2) than the free molecules, indicating greater electrophilic character of model clusters, and nucleophiles behavior of the free molecules.

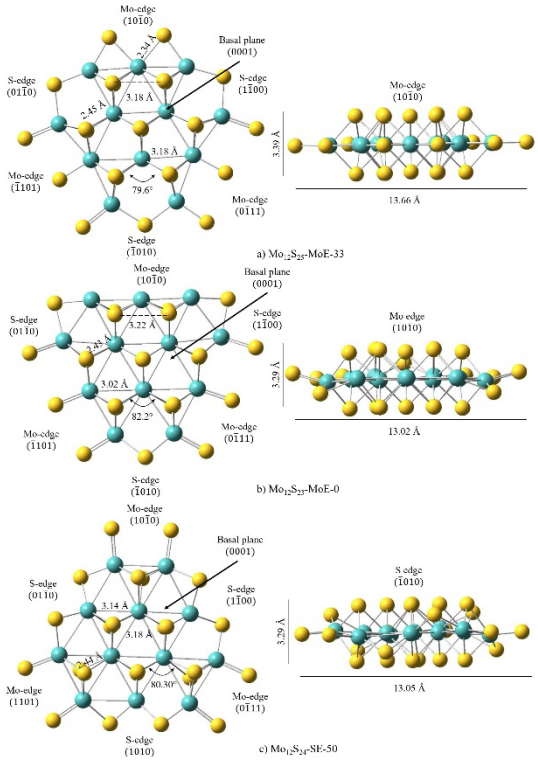

Fig. 4. Optimized structures for the model clusters, with average bond lengths and bond angles indicated. Yellow and cyan balls represent S and Mo atoms, respectively.

J. Mex. Chem. Soc. **2026**, *70(1):e2498*
Regular Issue

ISSN-e 2594-0317

Adsorbed molecules in the HDS of 4,6-DMDBT

Hydrogen activation

The spontaneity H_2 dissociative adsorption is analyzed from the corrected free energy at 60 bar H_2. The analysis and calculation of the adsorption energy correction are presented in Section S5 of the SI. Fig. 5 shows the hydrogen activation steps in both pathways, including the optimized structures of the species involved, together with their corrected adsorption energies and equilibrium constants. In Fig. 5**(a)** and 5**(b)**, (2H)•$Mo_{12}S_{25}$-MoE-33 and (2H)•$Mo_{12}S_{24}$-SE-50 systems are the dissociation products of H_2, forming two S-H groups on $MoS_{12}S_{25}$-MoE-33 and on $MoS_{12}S_{24}$-SE-50, respectively. During hydrogen activation, S atoms that form S-H groups show an increase in their partial charges in both pathways. For example, the partial charges on the S26 and S19 atoms of the $Mo_{12}S_{24}$-SE-50 cluster increase from -0.18 *e* to -0.11 *e* during HYDS pathway (Fig. 5**(b)**). The adsorption energy correction, $(\Delta G_{ad})_{H_2 corr}$, indicates that H_2 dissociation in (2H)•$Mo_{12}S_{25}$-MoE-33 (-0.79 eV) and (2H)•$Mo_{12}S_{24}$-SE-50 (-1.08 eV) is thermodynamically feasible at 60 bar of H_2 partial pressure.

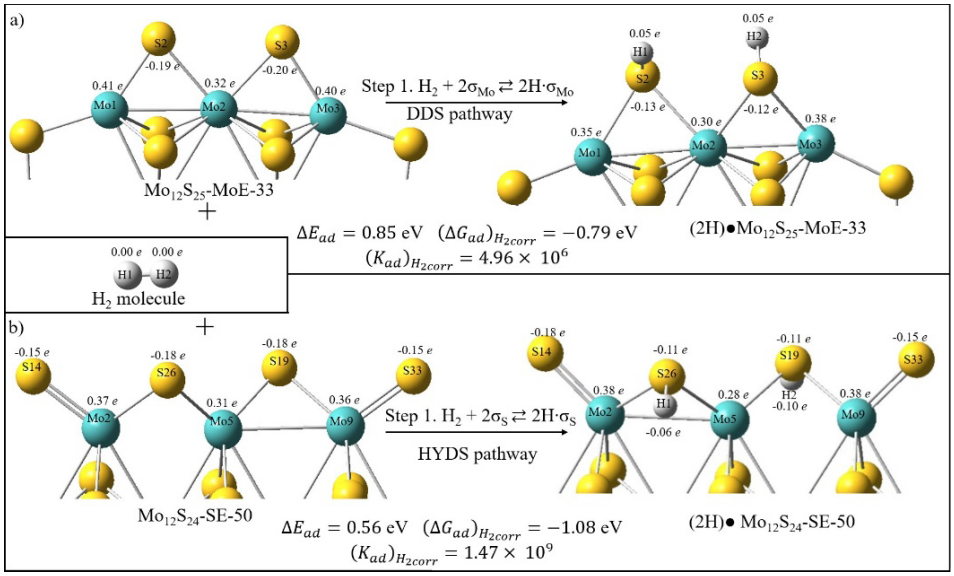

Fig. 5. Optimized structures of **(a)** the H_2 molecule and model clusters for H_2 activation, **(b)** activated hydrogen at the Mo-edge, and **(c)** activated hydrogen at the S-edge. Corrected Gibbs energy and equilibrium constants are at 593.15 K and 60 bar H_2 partial pressure.

σ-perpendicular adsorption modes in the DDS pathway

Fig. 6 shows the most important section of the Mo-edge structures for the σ-perpendicular adsorption modes of 4,6-DMDBT, 4,6-DMDHDBT, 3,3'-DMBPT and H_2S over the Mo atoms representing the CUS in the $Mo_{12}S_{23}$-MoE-0 cluster. Full optimized structures of adsorption modes are reported in Section S6 and presented in Fig. S4 of the SI.

The bond length between the S1 atom of the sulfur-containing molecules and the Mo2 atom of the cluster (r_{S1-Mo2}) is related to the strength of the σ-bond formed between these atoms. The relative chemisorption strength follows the order: 3,3'-DMBPT > H_2S ≈ 4,6-DMDBT > 4,6-DMDHDBT (Fig. 6). For chemisorbed 4,6-DMDBT (Fig. 6b), the r_{S1-Mo2} is 2.36 Å and is comparable to the reported S-Mo bond length (2.37 Å) [52], confirming the S1-Mo2 bond formation. The 4,6-DMDHDBT intermediate has the smallest S1-Mo2 bond length (2.32 Å), indicating a strong interaction between these atoms, whereas 3,3'-DMBPT exhibits the longest r_{S1-Mo2} length (2.45 Å), suggesting a weaker interaction.

J. Mex. Chem. Soc. **2026**, *70(1):e2498*
Regular Issue

ISSN-e 2594-0317

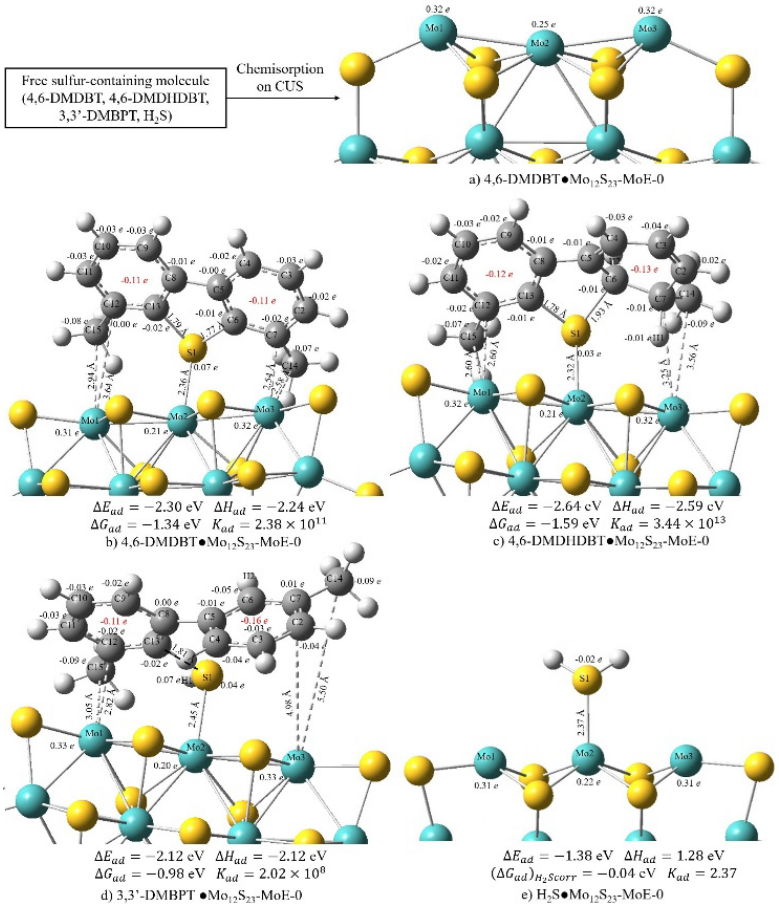

Fig. 6. σ-perpendicular adsorption modes of sulfur-containing molecules involved in the DDS pathway on the CUS of $Mo_{12}S_{23}$-MoE-0 in the 4,6-DMDBT HDS. Corrected Gibbs energy and equilibrium constants are reported at 593.15 K and 10^{-6} bar H_2S. **(a)** $Mo_{12}S_{23}$-MoE-0 cluster, **(b)** chemisorbed 4,6-DMDBT, **(c)** chemisorbed 4,6-DMDHDBT, **(d)** chemisorbed 3,3'DMBPT, and **(e)** chemisorbed H_2S. Red numbers indicate the total partial charges of the aromatic C atoms.

Based on the fact that the S and C atoms in a S-C bond of sulfur-containing aromatic molecules exhibit pronounced nucleophilic character and is susceptible to attack by dissociated hydrogen, an elongated S-C bond length may serve as an indicator of the ease with which hydrogenolysis occurs. Therefore, the S1-C6 bond length (r_{S1-C6}) is associated with susceptibility to bond scission during hydrogen transfer, while the S1-C13 bond length (r_{S1-C13}) is related to the ease of bond cleavage during hydrogenolysis reactions; a longer bond length implies weaker bond strength. Table 4 compares r_{S1-C6} and r_{S1-C13} lengths between the free sulfur-containing molecules and chemisorbed molecules with σ-perpendicular adsorption modes. The r_{S1-C6} lengths of chemisorbed molecules have the same order than free molecules (3,3'-DMBPT > 4,6-DMDHDBT > 4,6-DMDBT). The r_{S1-C6} lengths of the chemisorbed and free molecules are very similar, except for 4,6-DMDHDBT. Chemisorbed 4,6-DMDHDBT exhibits an large r_{S1-C6} (1.93 Å), about 5 % larger than that of the free molecule and exceeding the reported r_{S-C} of ethanethiol (1.82 Å) [53]. Therefore, the interaction of the sulfur atom with the CUS weakens the S-C bond of 4,6-DMDHDBT, suggesting a facilitated formation of 3,3'-DMBPT. This is explained by a change in the hybridization of the C6 atom from sp^2 to sp^3 during their formation.

http://dx.doi.org/10.29356/jmcs.v70i1.2498

J. Mex. Chem. Soc. **2026**, *70(1):e2498*
Regular Issue

ISSN-e 2594-0317

Table 4. Comparison of the S1-C6 and S1-C13 bond lengths between free and chemisorbed molecules on the CUS of $Mo_{12}S_{23}$-MoE-0.

Molecule	Free			Adsorbed on CUS		
	r_{S1-C6} (Å)	r_{S1-C13} (Å)	q_{S1} (e)	r_{S1-C6} (Å)	r_{S1-C13} (Å)	q_{S1} (e)
4,6-DMDBT	1.75	1.75	0.05	1.77	1.79	0.07
4,6-DMDHDBT	1.84	1.76	0.01	1.93	1.78	0.03
3,3'-DMBPT	3.12	1.78	-0.03	3.12	1.81	0.04
4,6-DMTHDBT	1.75	1.74	0.05	1.78	1.76	0.07
4,6-DMHHDBT	1.85	1.77	-0.01	1.88	1.78	0.04
Molecule	**Free**			**Adsorbed on CUS**		
	q_{A1} (e)	q_{A2} (e)		q_{A1} (e)	q_{A2} (e)	
4,6-DMDBT	-0.18	-0.18		-0.11	-0.11	
4,6-DMDHDBT	-0.18	-0.18		-0.13	-0.12	
3,3'-DMBPT	-0.18	-0.18		-0.16	-0.11	
4,6-DMTHDBT	-0.22	-0.21		-0.16	-0.12	
4,6-DMHHDBT	-0.22	-0.20		-0.20	-0.12	

The r_{S1-C13} lengths of chemisorbed molecules (Table 4) are longer than in free molecules. The r_{S1-C13} lengths of chemisorbed 3,3'-DMBPT (1.81 Å) is equal to the S-C bond length of ethanethiol, representing a 1.7 % increase compared with the free molecule (1.78 Å). This shows that the S1-C13 bond of chemisorbed 3,3'-DMBPT is weakened through interaction with CUS. The S1-C13 bond of chemisorbed 3,3'-DMBPT is not as weak as the S1-C6 bond of 4,6-DMDHDBT, therefore scission of the S1-C13 bond of chemisorbed 3,3'-DMBPT is expected to be slower. Additional properties (C7-Mo3 and C14-Mo3 bond lengths, μ, η, IP and EA) are discussed in section S7 of the SI.

Table 4 presents a comparison between the atomic partial charges (q_α) for the S1, A1 and A2 nucleophilic centers in free and chemisorbed molecules on the CUS, thereby enables the analysis of charge transfer during adsorption. The q_{S1} value of the molecules increases during adsorption due to charge transfer from S1 to the Mo2 atom (e.g., for 4,6-DMDBT adsorption on the CUS of $Mo_{12}S_{23}$-MoE-0: S1 from 0.05 e to 0.07 e, Mo2 from 0.25 e to 0.21 e; Fig. 6). Similarly, the total partial charge for each A1 and A2 centers of free molecules indicates electron transfer from these rings and the $Mo_{12}S_{23}$-MoE-0 cluster (e.g., for 4,6-DMDBT adsorption: A1 from -0.18 e to -0.11 e; Table 4). These results reveal significant interactions of A1 and A2 with the CUS.

Low Gibbs energy values of adsorption (ΔG_{ad}) or high adsorption constant values (K_{ad}) indicate a high adsorption capacity for a molecule under HDS conditions. ΔE_{ad}, ΔH_{ad}, ΔG_{ad} and K_{ad} of the adsorption modes involved during the DDS pathway are presented in Fig. 6. The K_{ad} constants present the following order 4,6-DMDHDBT > 4,6-DMDBT > 3,3'-DMBPT > H_2S. Therefore the 4,6-DMDHDBT molecule ($K_{ad} = 3.44 \times 10^{13}$) is strongly chemisorbed at HDS conditions. According to [54], the S-C bond scission is facilitated by a strong chemisorption between the S atom and a sulfur vacancy on the Mo-edge, suggesting that hydrogen transfer is not the rate-limiting step. The structural parameters and the equilibrium constants reveal that 3,3'-DMBPT is adsorbed less strongly than 4,6-DMDBT and 4,6-DMDHDBT.

http://dx.doi.org/10.29356/jmcs.v70i1.2498

J. Mex. Chem. Soc. **2026**, *70(1):e2498*
Regular Issue

ISSN-e 2594-0317

Experimentally, 3,3'-DMBPT is not observed as a product, which can be explained because the adsorption constant is sufficiently high ($K_{ad} = 2.02 \times 10^8$) to indicate that desorption is not thermodynamically favorable. The low K_{ad} value for 3,3'-DMBPT, compared to those of 4,6-DMDBT and 4,6-DMDHDBT, suggests that the hydrogenolysis of 3,3'-DMBPT may be part of the controlling reaction steps. The $(\Delta G_{ad})_{H_2Scorr}$ energy was calculated at 10^{-6} bar of H_2S partial pressure, and the $(K_{ad})_{H_2Scorr}$ equilibrium constant is low (2.37), therefore, H_2S desorption is likely. Section S8 of the SI provides the analysis and calculation of the $(\Delta G_{ad})_{H_2Scorr}$ energy and the $(K_{ad})_{H_2Scorr}$ equilibrium constant.

Table 5 presents the $\varepsilon_{HOMO-LUMO}$ gaps and ω indices for the molecular σ-perpendicular modes. The HOMO and LUMO orbitals for the σ-perpendicular modes involved in the DDS pathway are depicted in Fig. S5 in the Section S7 of the SI. The HOMO-LUMO gap indicates differences in reactivity among molecules of similar nature; lower values imply greater reactivity [55]. Since the sulfur-containing molecules studied here do not differ significantly, the criterion relating $\varepsilon_{HOMO-LUMO}$ to reactivity will be applied. For the adsorption modes involved in surface reactions, excluding the H_2S adsorption mode and hydrogen activation, the band gap order is as follows: 3,3'-DMBPT•$Mo_{12}S_{23}$-MoE-0 > 4,6-DMDBT•$Mo_{12}S_{23}$-MoE-0 > $Mo_{12}S_{23}$-MoE-0 > 4,6-DMDHDBT•$Mo_{12}S_{23}$-MoE-0. The chemisorbed 3,3′-DMBPT exhibits the highest band gap value (0.33 eV), whereas 4,6-DMDHDBT exhibits the lowest (0.27 eV), suggesting that the hydrogenation reaction of 3,3′-DMBPT is the most difficult, while hydrogen transfer is the most facile process. This analysis suggests that hydrogenolysis of 3,3'-DMBPT may be the rate-limiting step, with hydrogenation of 4,6-DMDBT playing a secondary role.

During hydrogen activation, the value of ω for (2H)•$Mo_{12}S_{25}$-MoE-33 (10.12 eV) shows that its electrophilic character increases with respect to that of $Mo_{12}S_{25}$-MoE-33 (8.97 eV, Table 2). On the other hand, the ω index of chemisorbed molecules on $Mo_{12}S_{23}$-MoE-0 follows the order: H_2S•$Mo_{12}S_{23}$-MoE-0 > $Mo_{12}S_{23}$-MoE-0 > 3,3'-DMBPT•$Mo_{12}S_{23}$-MoE-0 > 4,6-DMDBT•$Mo_{12}S_{23}$-MoE-0 ≈ 4,6-DMDHDBT•$Mo_{12}S_{23}$-MoE-0. These results reveal that 4,6-DMDHDBT•$Mo_{12}S_{23}$-MoE-0 ($\omega = 8.02$ eV) and 4,6-DMDBT•$Mo_{12}S_{23}$-MoE-0 modes ($\omega = 8.03$ eV) exhibit similar nucleophilic character, these modes have more nucleophilic character and are more reactive for hydrogenation than 3,3'-DMBPT•$Mo_{12}S_{23}$-MoE-0 ($\omega = 8.32$ eV).

Table 5. Global indices of chemisorbed modes on the active sites in the DDS pathway.

Chemisorbed mode	$\varepsilon_{HOMO-LUMO}$ **(eV)**	ω **(eV)**
$Mo_{12}S_{25}$-MoE-33	0.64(α)/0.31(β)	8.97
(2H)•$Mo_{12}S_{25}$-MoE-33	0.002	10.12
$Mo_{12}S_{23}$-MoE-0	0.29	8.61
4,6-DMDBT•$Mo_{12}S_{23}$-MoE-0	0.30	8.03
4,6-DMDHDBT•$Mo_{12}S_{23}$-MoE-0	0.27	8.02
3,3'-DMBPT•$Mo_{12}S_{23}$-MoE-0	0.33	8.32
H_2S•$Mo_{12}S_{23}$-MoE-0	0.20	9.67

Fig. 7 shows the surface reaction steps of the DDS pathway for 4,6-DMDBT together with ΔE_0, ΔH_R, ΔG_R, and K_{eq} at 593.15 K and 86 atm, as well as $(\Delta G_R)_{H_2S,corr}$ and $\left(K_{eq}\right)_{H_2Scorr}$ of H_2S desorption.

The 4,6-DMDBT adsorption and hydrogen activation steps are not shown in Fig. 7. At HDS operating conditions, equilibrium constants (considering the correction) follow the order: step 5

J. Mex. Chem. Soc. **2026**, *70(1):e2498*
Regular Issue

ISSN-e 2594-0317

(hydrogenolysis of 3,3'-DMBPT) > step 2 (adsorption of 4,6-DMDBT, Fig. 6) > step 1 (hydrogen activation, Fig. 5) > step 3 (4,6-DMDHDBT formation) > step 4 (transfer of hydrogen) > step 1 (H_2S desorption). These results show that the equilibrium constants for 4,6-DMDBT hydrogenation and 4,6-DMDHDBT formation ($K_{eq} = 2.16 \times 10^4$), and 3,3'-DMBPT hydrogenolysis ($K_{eq} = 3.74 \times 10^{13}$) surface reactions are very high compared with the corresponding values for the reactions without molecule-catalyst interactions ($K_{eq} = 1.23 \times 10^{-9}$ for 4,6-DMDHDBT formation and $K_{eq} = 2.62 \times 10^4$ for 3,3'-DMBPT hydrogenolysis). However, the equilibrium constant of catalytic hydrogen transfer ($K_{eq} = 6.98$) decreases compared with the reaction without molecule-cluster interaction ($K_{eq} = 1.19 \times 10^6$). Catalytic hydrogenation and hydrogenolysis reactions are practically irreversible, whereas the hydrogen transfer reaction is reversible, tending to form 3,3'-DMBPT.

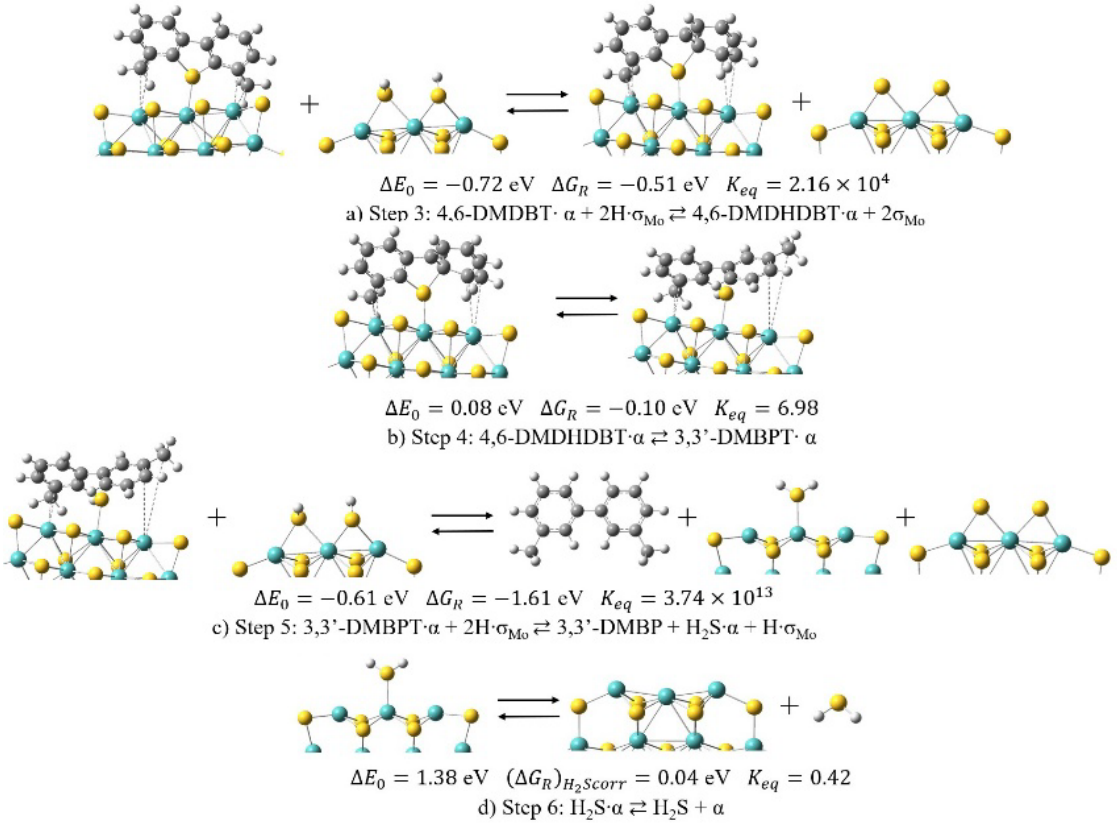

Fig. 7. Reaction steps in the DDS pathway for the HDS of 4,6-DMDBT. Corrected Gibbs energies and equilibrium constants at 593.15 K and 60 bar H_2 partial pressure, and 10^{-6} bar H_2S.

Adsorbed molecules modes in the HYDS pathway

Fig. 8 exhibits the lowest energy structures for the π-planar adsorption modes on brim sites for relevant molecules involved in the HYDS pathway. The distance (r_{M-C}, see Fig. 8) between the A2 ring and the (0001) basal plane of $Mo_{12}S_{24}$-SE-50 was calculated as the average distance between the C atoms of the A2 ring and the S atoms of the basal plane. The r_{M-C} has the order: 3,3'-MCHT•$Mo_{12}S_{24}$-SE-50 > 4,6-DMHHDBT•$Mo_{12}S_{24}$-SE-50 > 4,6-DMDBT•$Mo_{12}S_{24}$-SE-50 > 4,6-DMTHDBT•$Mo_{12}S_{24}$-SE-50. This distance reflects the interaction strength between the A2-ring and the cluster $Mo_{12}S_{24}$-SE-50, but it does not completely describe the adsorption capacity of the molecules, since unlike the other molecules, 4,6-DMDBT has two aromatic rings that interact with the cluster, promoting stronger adsorption.

http://dx.doi.org/10.29356/jmcs.v70i1.2498

J. Mex. Chem. Soc. **2026**, *70(1):e2498*
Regular Issue

ISSN-e 2594-0317

At HDS conditions K_{ad} shows the order: 4,6-DMDBT•$Mo_{12}S_{24}$-SE-50 > 4,6-DMHHDBT•$Mo_{12}S_{24}$-SE-50 ≈ 4,6-DMTHDBT•$Mo_{12}S_{24}$-SE-50 > 3,3'-MCHT•$Mo_{12}S_{24}$-SE-50. This order can be explained because the number of π-orbitals of the molecule that interact with the cluster decreases during the hydrogenation. The K_{ad} predicts that the adsorption capacity of 4,6-DMHHDBT (2.21) is similar to that of 4,6-DMTHDBT (2.15). This can be explained because in the HOMO orbital of 4,6-DMHHDBT there shows higher electron density on the S atom, which slightly contributes to the adsorption on the brim site. The ΔG_{ad} values are low (e.g., for 4,6-DMDBT, it is -0.11 eV or -2.59 kcal/mol, corresponding to a physisorption process [56]), such adsorptions can be considered reversible. This shows that the 4,6-DMDBT, 4,6-DMTHDBT and 4,6-DMHHDBT species can desorb from the brim sites, diffuse, and then adsorb on the CUS to be desulfurized.

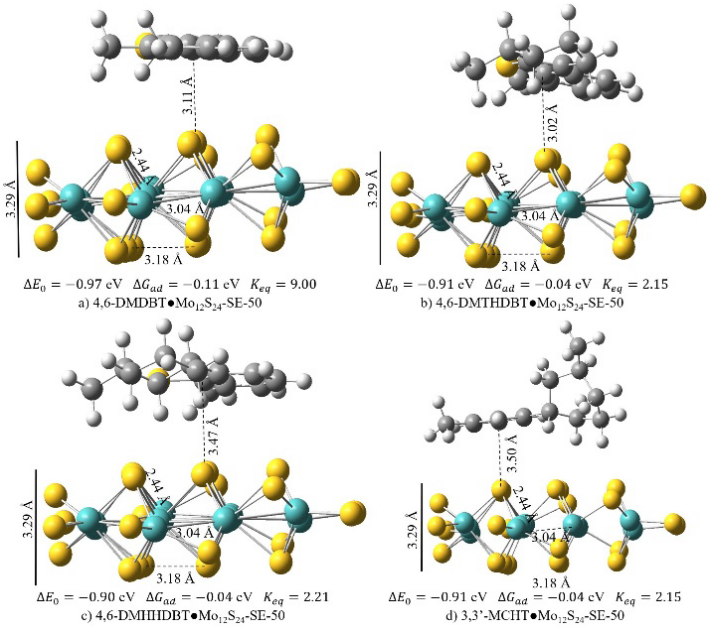

Fig. 8. π-planar adsorption modes on brim active sites of the $Mo_{12}S_{24}$-SE-50 cluster.

Optimized structures of the σ-perpendicular adsorption modes of 4,6-DMTHDBT and 4,6-DMHHDBT on the CUS of the $Mo_{12}S_{23}$-MoE-0 cluster are presented in Fig. 9. The r_{S1-Mo2} decreases as follows: 4,6-DMDBT•$Mo_{12}S_{23}$-MoE-0 ≈ 4,6-DMTHDBT•$Mo_{12}S_{23}$-MoE-0 > 4,6-DMHHDBT•$Mo_{12}S_{23}$-MoE-0. This reveals that there is more interaction between the S1 atom of 4,6-DMHHDBT and the Mo2 atom of the cluster than in the other molecules. The r_{S1-Mo2} of 4,6-DMHHDBT (2.33 Å) is only slightly larger than that in the 4,6-DMDHDBT intermediate (2.32 Å) of the DDS path, showing similar S1-Mo2 interaction. The $r_{C12-Mo1}$ of 4,6-DMHHDBT (2.55 Å) points that a stronger A2 non-hydrogenated ring interaction with the cluster than that exhibited by 4,6-DMTHDBT (2.63 Å) and 4,6-DMDHDBT (2.60 Å). The r_{S1-C6} increases int the order: 4,6-DMDBT•$Mo_{12}S_{23}$-MoE-0 ≈ 4,6-DMTHDBT•$Mo_{12}S_{23}$-MoE-0 < 4,6-DMHHDBT•$Mo_{12}S_{23}$-MoE-0. The r_{S1-C6} lengths of 4,6-DMDBT (1.77 Å) and 4,6-DMTHDBT (1.78 Å) are similar; therefore, as this bond is not weakened, further hydrogenation is necessary for the S-C bond scission. The r_{S1-C6} length of 4,6-DMHHDBT•$Mo_{12}S_{23}$-MoE-0 (1.88 Å) is longer than the S-C bond in ethanethiol but shorter than that in 4,6-DMDHDBT (1.93 Å). This suggests that the S1-C6 bond can be weakened relatively easily and that the bond in 4,6-DMDHDBT is weaker than that in 4,6-DMHHDBT.

http://dx.doi.org/10.29356/jmcs.v70i1.2498

J. Mex. Chem. Soc. **2026**, *70(1):e2498*
Regular Issue

ISSN-e 2594-0317

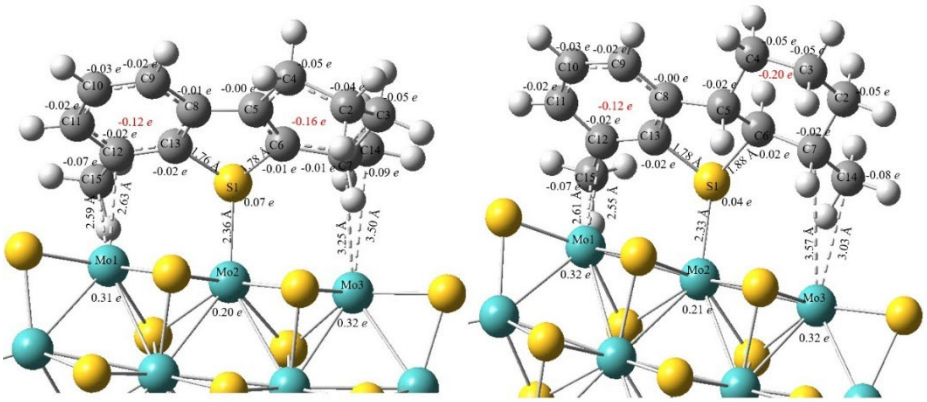

Fig. 9. σ-perpendicular adsorption modes on the CUS of the $Mo_{12}S_{23}$-MoE-0 cluster. Red values indicate the total charges of the A1 and A2 centers.

The partial charges of free and chemisorbed molecules of 4,6-DMTHDBT and 4,6-DMHHDBT are shown in Table 4. The change in q_{S1} charges in 4,6-DMTHDBT from the free to the chemisorbed molecule show the same change as 4,6-DMDBT (from 0.05 *e* to 0.07 *e*), indicating that the S1 atoms of these molecules donate similar electron densities to the CUS. The q_{S1} charges of 4,6-DMHHDBT reflects a slight change between the free and the chemisorbed molecule (from 0.05 *e* to 0.04 *e*). The A2 rings of 4,6-DMTHDBT and 4,6-DMHHDBT exhibit a greater change in charges between free and chemisorbed molecules, suggesting that the π-orbitals have the greatest contribution from the active site-molecule interaction (for A2 of both molecules the partial charge varies from -0.21 *e* to -0.12 *e*). For 4,6-DMHHDBT the A1 ring has a slight change (from -0.22 *e* to -0.20 *e*), suggesting that this center transfers only small amount electron density to the cluster. For 4,6-DMTHDBT, the A1 ring shows a larger change in charges (from -0.22 *e* to -0.16 *e*) than the A1 ring of 4,6-DMHHDBT, indicating that the A1 ring of 4,6-DMTHDBT donates more electron density to the cluster.

Fig. 9 shows ΔE_{ad}, ΔH_{ad}, ΔG_{ad} and K_{ad}, the equilibrium adsorption constants follow the order: 4,6-DMHHDBT > 4,6-DMDBT > 4,6-DMTHDBT. According to K_{ad}, 4,6-DMDBT (2.38×10^{11}) adsorbs more strongly than 4,6-DMTHDBT (1.70×10^{11}), despite its longer S1-Mo2 bond length, due to the interaction of the two aromatic rings of 4,6-DMDBT with the Mo1 and Mo3 atoms. The 4,6-DMHHDBT intermediate (1.39×10^{14}) adsorbs more strongly than 4,6-DMDBT and 4,6-DMTHDBT, because of stronger interactions between the S1 atom and the A2 ring with the cluster. According to K_{ad}, 4,6-DMHHDBT adsorbs more strongly than 4,6-DMDHDBT (3.44×10^{13}), however, this does not necessarily imply that its S1-C6 bond scission is faster than 4,6-DMDHDBT, as 4,6-DMDHDBT has weaker S1-C6 bond. An increased S-C bond length and strong adsorption of the S atom are necessary to facilitate rapid S-C bond cleavage. Thus, the S1-C6 bond of 4,6-DMHHDBT may breaks more slowly than that of 4,6-DMDHDBT. This does not necessarily imply that H_2S formation from 4,6-DMHHDBT is slower since a 3,3'-methylcyclohexyltoluenethiol species with weaker S1-C6 bond may be formed.

Fig. 10 presents the reaction energies and equilibrium constants for selected HYDS steps, excluding hydrogen activation (Fig. 5), adsorption on CUS (Fig. 9), and H_2S desorption (Fig. 6) steps. The equilibrium constants in the HYDS pathway follow the order: step 10 > step 3 > step 9 > step 8 > step 7 > step 1 > step 4 > step 2 > step 5 > step 6 > step 11, see Table 1. The 4,6-DMHHDBT•$Mo_{12}S_{23}$-MoE-0 formation and its hydrogenolysis reactions (step 9 and 10, respectively, Fig. 10) on the CUS of the $Mo_{12}S_{23}$-MoE-0 cluster are the more thermodynamically favorable steps for the HYDS pathway.

J. Mex. Chem. Soc. **2026**, *70(1):e2498*
Regular Issue

ISSN-e 2594-0317

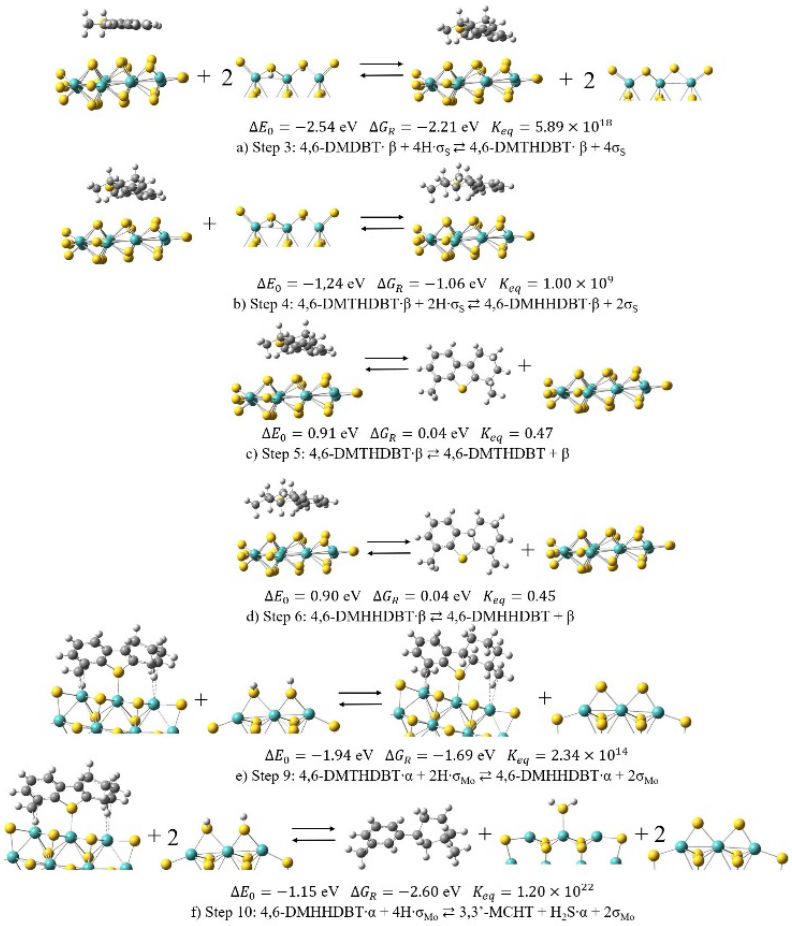

Fig. 10. Reaction steps in the HYDS pathway for HDS of 4,6-DMDBT. Corrected Gibbs energy and equilibrium constants at 593.15 K and 60 bar H_2 partial pressure, and 10^{-6} bar H_2S.

Correlations of energy properties for free and chemisorbed molecules

The multilinear relationships of the structural, electronic, and energy properties between free and chemisorbed molecules involved in the DDS and HYDS presented here allow the perdition of the behavior of molecules of similar nature interacting with the catalytic surface.

Consider the following multilinear equation:

$$y = \beta_0 + \sum_{i=1}^{n} \beta_i x_i \tag{9}$$

where y is a property of the chemisorbed molecules, x_i is a property of the free molecules, n is the number of the free molecule properties, β_i are multilinear coefficients and β_0 is the multilinear independent coefficient.

The x_i properties of each proposed correlation were selected based on several tests involving different reactivity indices and properties of the free molecules. The indices ω, ω_{S1}^{-}, ω_{A1}^{-} and ω_{A2}^{-} are particularly significant in describing the properties governing adsorption processes at both sites, as they serve as indicators of the nucleophilic character of the entire molecule as well as its principal centers (S1, A1, and A2) individually. Based on the above and on the fact that nucleophilic centers interact to different degrees with the active sites, these indices of free molecules may be related with ΔE_{ad}, r_{S1-C6}, r_{S1-C13} and r_{S1-Mo2} bond lengths in the chemisorbed molecules.

http://dx.doi.org/10.29356/jmcs.v70i1.2498

J. Mex. Chem. Soc. **2026**, *70(1):e2498*
Regular Issue

ISSN-e 2594-0317

During σ-perpendicular adsorption, the S1-Mo2 bond is formed, accompanied by weak interactions between the aromatic rings of the molecules and the CUS site. When the S1-Mo2 bond is established, the *sp³* hybridization state of the S1 atom remains unchanged, and the S1-C6 and S1-C13 bonds are not expected to undergo significant variation. Consequently, the bond lengths in the free molecules may serve as suitable indicators for describing those in the chemisorbed species.

Table 6 shows the multilinear relationships between structural and electronic properties of free and chemisorbed molecules during DDS, together with their multilinear coefficients and the coefficient of determination (R^2). The most important results are summarized below.

A multilinear relationship was found between r_{S1-C6} values in the chemisorbed molecules on the CUS of the $Mo_{12}S_{23}$-MoS-0 cluster and the r_{S1-C6} values and ω indices of the free molecules, as expressed in equation (10) of Table 6. The equation (10) was derived from the properties of the free molecules 4,6-DMDBT, 4,6-DMDHDBT, 4,6-DMTHDBT and 4,6-DMHHDBT. The intermediate 3,3'-DMBPT was excluded, since its S1 and C6 atoms are not bonded.

Table 6. Multilinear relationships of the structural and energy properties between free and chemisorbed molecules involved in the DDS.

$$r^{CM}_{S1-C6} = \beta_0 + \beta_1 r_{S1-C6} + \beta_2 \omega \quad (10)$$
$$r^{CM}_{S1-C13} = \beta_1 r_{S1-C13} + \beta_2 \omega^-_{S1} + \beta_3 \omega^-_{A1} + \beta_4 \omega^-_{A2} \quad (11)$$
$$r_{S1-Mo2} = \beta_0 + \beta_1 \omega^-_{S1} + \beta_2 \omega^-_{A1} + \beta_3 \omega^-_{A2} \quad (12)$$
$$\Delta E_{ad} = \beta_0 + \beta_1 \omega^-_{S1} + \beta_2 \omega^-_{A1} + \beta_3 \omega^-_{A2} \quad (13)$$
$$\Delta E^{Cat}_0 = \beta_0 + \beta_1 \omega + \beta_2 \Delta E^{NCat}_0 + \beta_3 \varepsilon_{HOMO-LUMO} \quad (14)$$

where the superscript CM indicates chemisorbed molecules.

Regression coefficients for the multilinear relationships

Equation	β_0	β_1	β_2	β_3	β_4	R^2
(17)	-0.7124	1.3655	0.0639			0.9162
(18)	0.0000	1.1094	0.0056	0.1789	-0.5940	0.9999
(19)	4.0030	-0.1618	1.2136	-5.1385		0.8442
(20)	6.07	-2.79	6.60	-25.35		0.9494
(21)	-12.4811	5.2836	-0.5351	0.9085		0.9757

The ω^-_{S1}, ω^-_{A1} and ω^-_{A2} indices and the r_{S1-C13} bond lengths of the free molecules were correlated with r_{S1-C13} lengths of the chemisorbed molecules according to equation (11). In (18), $\beta_0 = 0$ was selected because there were insufficient r_{S1-C13} values (4,6-DMDBT, 4,6-DMDHDBT, 3,3'-DMDBT, 4,6-DMTHDBT and 4,6-DMHHDBT) to fit all multilinear coefficients ($\beta_0, \beta_1, \beta_2, \beta_3$ and β_4) of the selected variables ($r_{S1-C13}, \omega^-_{S1}, \omega^-_{A1}$ and ω^-_{A2}). By setting $\beta_0 = 0$, the multilinear relationship can be understood as the sum of the contributions of the bond length of the free molecule plus the contributions from catalyst interactions with the molecule nucleophilic centers. A comparison between the r_{S1-C6} and r_{S1-C13} calculated by DFT and the multilinear relationship is shown in Section S9 of the SI, showing maximum absolute errors of 0.86% and 1.5%, respectively.

The changes of the r_{S1-Mo2} distances of the 4,6-DMDHDBT•$Mo_{12}S_{23}$-MoS-0 system reflect the ability to donate electron density from the nucleophilic centers of the adsorbed molecule to the CUS. The r_{S1-Mo2} distance presented a multilinear relationship with the ω^-_{S1}, ω^-_{A1} and ω^-_{A2} indices of the free molecules, see equation (12) in Table 6.

It was proposed that the adsorption energies of σ-perpendicular adsorption at 0 K (ΔE_{ad}) of 4,6-DMDBT, 4,6-DMDHDBT, 3,3'-DMDBT, 4,6-DMTHDBT and 4,6-DMHHDBT are related to the ω^-_{S1}, ω^-_{A1}

J. Mex. Chem. Soc. **2026**, *70(1):e2498*
Regular Issue

ISSN-e 2594-0317

and ω_{A2}^{-} indices of the free molecules, as expressed in equation (13) of Table 6. The regression coefficients β_1, β_2 and β_3 in equation (13) quantify the variation in ΔE_{ad} resulting from changes in the nucleophilicity of the S1, A1 and A2 centers, respectively. A large negative coefficient indicates stronger interaction between its corresponding nucleophilic center with the CUS, enhancing the molecule ability to be adsorbed. The high negative value of the β_3 coefficient indicates that a decrease in the nucleophilic character of the A2 non-hydrogenated aromatic ring produces a significant decrease in the adsorption energy. Therefore, the π-orbitals of the A2 ring play an essential role in the adsorption steps of the hydrogenated species. In general, as the hydrogenation degree of the A1 aromatic ring is carried out (except for 4,6-DMDHDBT) the overall nucleophilic character of the molecules increases, owing to charge transfer from A1 to the A2 ring. The positive value of β_2 can be explained because the A1 center loses its nucleophilic character, charge is transferred to the S1 and A2 nucleophilic centers, thereby contributes to the adsorption.

The surface reaction energies are related to the ω and $\varepsilon_{HOMO-LUMO}$ of the free sulfur-containing reactants, and their corresponding reaction energies without molecule-catalyst interactions. The hydrogenation capacity of a molecule depends on its ability to donate or accept electron density from the environment. On the other hand, surface reaction energies in the absence of molecule-catalyst interactions (ΔE_0^{NCat}) may be regarded as the energy contribution arising from the structural changes between reactants and products. Accordingly, $\varepsilon_{HOMO-LUMO}$ and ΔE_0^{NCat} may be an adequate measure of the ease with which hydrogenation occurs. This multilinear relationship is presented in equation (14) in Table 6, and Table 7 shows a comparison between the results obtained by the multilinear relationship and those calculated by DFT. In Table 7, ΔE_0^{Cat} is reaction energy with interaction molecule-active site. The maximum error, 16.25 %, corresponds to the hydrogen transfer reaction, this is due to its low reaction energy (0.08 eV). However, the hydrogen transfer reaction energy is below the energy accuracy of the DFT (~0.05 eV), therefore the multilinear model satisfactorily predicts the reaction energies. The reaction without interaction molecule-active site of 4,6-DMDHDBT formation is endothermic ($\Delta E_0^{NCat} = 0.47$ eV). However, the 4,6-DMDHDBT formation energy with molecule-catalyst interactions is exothermic ($\Delta E_0^{Cat} = -0.72$ eV), highlighting the importance of the interaction between 4,6-DMDBT and the $Mo_{12}S_{23}$-MoE-0 cluster for this reaction step.

Table 7. Comparison of reaction energies obtained by DFT and multilinear relationship in the DDS pathway.

Reaction	ΔE_0^{DFT} (eV)	$\Delta E_0^{Multilinear}$ (eV)	% Absolute error
4,6-DMDBT + H_2 ⇌ 4,6-DMDHDBT	-0.72	-0.71	0.81
4,6-DMDHDBT ⇌ 3,3'-DMBPT	0.08	0.07	16.25
3,3'-DMBPT+ H_2 ⇌ 3,3'-DMBP + H_2S	-0.61	-0.67	10.34
4,6-DMTHDBT + H_2 ⇌ 4,6-DMHHDBT	-1.69	-1.56	7.98
4,6-DMHHDBT + 2H_2 ⇌ 3,3'-MCHT+ H_2S	-2.60	-2.66	2.49

ΔE_0^{Cat} and ΔE_0^{NCat} are reaction energies with and without interaction molecule-catalyst.

Table 8 presents the results of the multilinear relationships of r_{M-C} and ΔE_{ad} for the π-adsorption modes associated with the HYDS pathway on the brim sites of the $Mo_{12}S_{24}$-SE-50 cluster. The π-planar adsorption modes of 4,6-DMDBT, 4,6-DMTHDBT, 4,6-DMHHDBT, and 3,3'-MCHT were considered for the multilinear relationship analysis. The r_{M-C} distances between the molecules and the $Mo_{12}S_{24}$-SE-50 cluster correlate with the nucleophilic centers A1, A2 and S1, according to equation (15). In contrast, the nucleophilic indices ω_{A1}^{-} and ω_{A2}^{-} of free molecules are sufficient to predict ΔE_{ad} in π-adsorption modes (see equation (16) of Table 8). Moreover, the regression coefficients β_1 and β_2 in equation (16) reveal that the π-orbital interactions of the A1 nucleophilic centers with the brim site are more significant than the A2 nucleophilic centers, because the A1 center loses its nucleophilic character during the hydrogenation.

http://dx.doi.org/10.29356/jmcs.v70i1.2498

J. Mex. Chem. Soc. **2026**, *70(1):e2498*
Regular Issue

ISSN-e 2594-0317

Table 8. Multilinear relationships between structural and energy properties of free and adsorbed molecules involved in the HYDS pathway.

$$r_{M-C} = \beta_1\omega_{S1}^{-} + \beta_2\omega_{A1}^{-} + \beta_3\omega_{A2}^{-} \quad (15)$$
$$\Delta E_{ad} = \beta_0 + \beta_1\omega_{A1}^{-} + \beta_2\omega_{A2}^{-} \quad (16)$$

Regression coefficients for the multilinear relationships

Equation	β_0	β_1	β_2	β_3	Adjusted R^2
(22)	0.0000	3.4410	-2.9583	7.9456	0.9999
(23)	-1.2184	-0.4174	1.0660		0.9481

A multilinear relationship could not be established between the surface reaction energies in brim sites and the properties of free molecules, because only two data points were obtained for hydrogenation reaction energy (4,6-DMTHDBT and 4,6-DMHHDBT formation reactions). Therefore, further analysis of the hydrogenation and hydrogenolysis reactions in the HYDS pathway is required for various sulfur-containing molecules (e.g., DBT and 4-MDBT).

Linear trends are also observed between ZPE, E_{corr}, H_{corr}, and G_{corr} for the sulfur-containing molecules (4,6-DMDBT, 4,6-DMDHDBT, 3,3'-DMBPT, 4,6-DMTHDBT, 4,6-DMHHDBT and H_2S) and their σ-perpendicular and π-adsorption modes. The results of the linear relationships of energy corrections are shown in Table 9 and Section S10 of the SI.

The R^2 coefficients indicate nearly perfect linear relationships between the energy corrections of the free and chemisorbed species on $Mo_{12}S_{23}$-MoE-0. These results can be explained because the dominant vibrational frequencies which are arise primarily from the atoms of the adsorbed molecule rather than those of the model cluster. These results are of great importance given the high computational cost of calculating vibrational frequencies and the energy corrections of the adsorbed species. In the regression analysis, the H_2S•$Mo_{12}S_{23}$-MoE-0 mode and the $Mo_{12}S_{23}$-MoE-0 and $Mo_{12}S_{24}$-SE-50 clusters were included, suggesting that the dominant vibrational frequencies of the molecules are associated with the sulfur atom. Therefore, this type of relationship could be investigated in the future for sulfur-containing species of similar structure with the same adsorption mode.

Table 9. Multilinear relationships for correction of energies in the DDS and HYDS pathway.

$$ZPE^{Chemisorbed\ Molecule} = \beta_0 + \beta_1 ZPE^{Free\ Molecule} \quad (17)$$
$$E_{corr}^{Chemisorbed\ Molecule} = \beta_0 + \beta_1 E_{corr}^{Free\ Molecule} \quad (18)$$
$$H_{corr}^{Chemisorbed\ Molecule} = \beta_0 + \beta_1 H_{corr}^{Free\ Molecule} \quad (19)$$
$$G_{corr}^{Chemisorbed\ Molecule} = \beta_0 + \beta_1 G_{corr}^{Free\ Molecule} \quad (20)$$

Equation	DDS pathway			HYDS pathway		
	β_0	β_1	R^2	β_0	β_1	R^2
(22)	0.9894	1.6396	1.0000	0.9990	1.6822	1.0000
(23)	0.9940	5.5639	0.9999	0.9988	5.7603	1.0000
(24)	0.9940	5.5641	0.9999	0.9988	5.7603	1.0000
(25)	1.0852	-4.6311	0.9987	1.0037	-4.6162	1.0000

http://dx.doi.org/10.29356/jmcs.v70i1.2498

J. Mex. Chem. Soc. **2026**, *70(1):e2498*
Regular Issue

ISSN-e 2594-0317

Conclusions

Free and adsorbed molecules on CUS and brim sites involved in the reaction steps of the HYDS and DDS pathways for HDS of 4,6-DBDMDBT were studied at the UPBE-GGA/DEF2TZVP level of theory. Adsorption steps of sulfur-containing molecules, as well as hydrogenation and hydrogenolysis reactions for the DDS and HYDS pathways were characterized by their adsorption and surface reaction energies. Multilinear relationships were found between the structural and energy properties of free and adsorbed molecules on CUS and brim sites. Specially, the condensed nucleophilicity indices for the main centers (ω_{S1}^{-}, ω_{A1}^{-} and ω_{A2}^{-}) of free sulfur-containing molecules can be used to construct multilinear relationships to estimate the properties of the adsorbed molecules. The approach used here considers that the nucleophilic centers of free molecules contribute independently to the molecule-active site interaction to predict the chemical reactivity of the HDS reaction steps. This approach has not been used previously. Additionally, CDFT has not previously been applied to study the reaction intermediates of the DDS and HYDS pathways (4,6-DMDHDBT, 3,3'DMBPT, 4,6-DMTHDBT and 4,6-DMHHDBT) and the associated adsorption, hydrogenation, hydrogen transfer, and hydrogenolysis reaction steps.

Based on the above, our conclusions are the following:

The S1-C6 bond length of chemisorbed molecules in σ-perpendicular modes on the CUS can be predicted through a multilinear relationship involving ω index and S1-C6 bond lengths of free molecules. This occurs because interactions of the S1, A1, and A2 nucleophilic centers with the CUS increase the S1-C6 bond length in chemisorbed molecules, particularly in the 4,6-DMDHDBT molecule, thereby facilitating bond scission and the hydrogen transfer reaction.

The S1-C13 bond length of the non-hydrogenated aromatic ring A2 in free molecules cannot alone account for the S1-C13 bond length of adsorption σ-perpendicular modes. The interaction of the π-orbitals of the non-hydrogenated aromatic ring A2 with the CUS is essential for weakening the S1-C13 bond. Consequently, a multilinear relationship exists between the S1-C13 bond length of the chemisorbed species and the S1-C13 bond length and the condensed nucleophilicity indices of the S1, A1 and A2 centers of the free molecules.

The S1-Mo2 bond length and adsorption energy of the molecules for a σ-perpendicular adsorption on the CUS can be expressed through multilinear relationships whit condensate nucleophilicity indices of the S1, A1 and A2 centers. The large S1-Mo2 bond length (2.45 Å), high band gap (0.33 eV), and adsorption energy (-2.12 eV) of 3,3'-DMBPT, relative to other molecules, suggest that hydrogenolysis of 3,3'-DMBPT is the reaction-controlling step in the DDS pathway, without accounting for steric hindrance in the adsorption.

A multilinear relationship with $\varepsilon_{HOMO-LUMO}, \omega$ and ΔE_0^{NCat} for free sulfur-containing molecules adequately represents surface reaction energies proposed on the CUS for both pathways.

Adsorption energies at 0 K and vacuum ΔE_{ad} for the π-planar modes of 4,6-DMDBT, 4,6-DMTHDBT, 4,6-DMHHDBT, and 3,3'-MCHT in brim sites, show that as the aromatic rings become saturated during the HYDS pathway, the adsorption becomes progressively less thermodynamically stable. Under HDS conditions (593.13 K and 85 atm), the adsorption of 4,6-DMTHDBT and 4,6-DMHHDBT on the brim sites is nearly athermic (-0.04 eV for both molecules), therefore desorption from the brim sites and followed by diffusion and adsorption on the CUS can occur. This is consistent with the experimental detection of 4,6-DMTHDBT and 4,6-DMHHDBT in the fluid phase.

The molecule-cluster distance (r_{M-C}) and adsorption energies for the π-planar adsorption of 4,6-DMDBT, 4,6-DMTHDBT, 4,6-DMHHDBT and 3,3'-MCHT exhibit a multilinear relationship with the ω_{S1}^{-}, ω_{A1}^{-} and ω_{A2}^{-} indices. Furthermore, the multilinear relationship of the adsorption energy indicates that the interactions of the π-orbitals of the A1 and A2 centers are highly important in the adsorption on the brim active sites.

An almost perfect linear relationship was observed for corrections at 593.13 K and 85 atm involving zero-point, thermal energy, enthalpy, and Gibbs energy between free molecules and their σ-perpendicular and π-planar adsorption modes on the CUS and brim active sites of model clusters. This result can be explained by the observation that the vibrational frequencies associated with the S-Mo bond between the free molecule and the $Mo_{12}S_{23}$-MoS-0 cluster in the σ-perpendicular mode are insignificant with respect to the vibrational frequencies of the unbonded atoms in the free molecule. In the case of the π-planar mode, the linear trend

J. Mex. Chem. Soc. **2026**, *70(1):e2498*
Regular Issue

ISSN-e 2594-0317

becomes more pronounced, since the molecule-cluster interactions are weak as the process corresponds to physisorption. These results enable rapid estimation of energy corrections for σ-perpendicular or π-planar adsorption modes.

Acknowledgements

We gratefully acknowledge financial support from DGAPA-PAPIIT IN-112021 and from FQ-UNAM PAIP-5000-9072. H. Martinez-Grimaldo acknowledges a PhD fellowship from CONACyT. M. Castro strongly acknowledges financial support provided by DGAPA-UNAM, under Project PAPIIT IN-100725, and from Facultad de Química UNAM, under the PAIP–FQ program. We are thankful to the Dirección General de Cómputo y de Tecnologías de la Información (DGTIC-UNAM) for providing access to supercomputing resources on the Miztli supercomputer; Project LANCAD-UNAM-DGTIC-063.

References

1. Rana, M. S.; Sámano, V.; Ancheyta, J.; Diaz, J. A. I. *Fuel.* **2007**, *86*, 1216–1231 DOI: https://doi.org/10.1016/j.fuel.2006.08.004
2. Stanislaus, A.; Marafi, A. M. J.; Rana, M. S. *Catal. Today.* **2010**, *153*, 1–68 DOI: https://doi.org/10.1016/j.cattod.2010.05.011
3. Brorson, M.; Carlsson, A.; Topsøe, H. *Catal. Today* **2007**, *123*, 31–36 DOI: https://doi.org/10.1016/j.cattod.2007.01.073.
4. Topsøe, H. The Role of Co–Mo–S Type Structures in Hydrotreating Catalysts. *Appl. Catal. Gen.* **2007**, *322*, 3–8 DOI: https://doi.org/10.1016/j.apcata.2007.01.002.
5. Houalla, M.; Nag, N. K.; Sapre, A. V.; Broderick, D. H.; Gates, B. C. Hydrodesulfurization of Dibenzothiophene Catalyzed by Sulfided CoO-MoO3γ-Al2O3: The Reaction Network. *AIChE J.* **1978**, *24* (6), 1015–1021 DOI: https://doi.org/10.1002/aic.690240611.
6. Ding, L.; Zhang, Z.; Zheng, Y.; Ring, Z.; Chen, J. Effect of Fluorine and Boron Modification on the HDS, HDN and HDA Activity of Hydrotreating Catalysts. *Appl. Catal. Gen.* **2006**, *301* (2), 241–250 DOI: https://doi.org/10.1016/j.apcata.2005.12.014.
7. Nicosia, D.; Prins, R. The Effect of Phosphate and Glycol on the Sulfidation Mechanism of CoMo/Al2O3 Hydrotreating Catalysts: An in Situ QEXAFS Study. *J. Catal.* **2005**, *231* (2), 259–268 DOI: https://doi.org/10.1016/j.jcat.2005.01.018.
8. Ramírez, J.; Sánchez-Minero, F. Support Effects in the Hydrotreatment of Model Molecules. *Catal. Today* **2008**, *130* (2), 267–271 DOI: https://doi.org/10.1016/j.cattod.2007.10.103.
9. Bai, Z.; Wang, L.; Cao, H.; Zhang, X.; Li, G. Symbiosis of 1 T and 2H Phases in the Basal Plane of Defective MoS2 Nanoflowers for Efficient Hydrodesulfurization. *Fuel* **2022**, *322*, 124252 DOI: https://doi.org/10.1016/j.fuel.2022.124252.
10. Wang, L.; Bai, Z.; Zhang, X.; Li, G. Co-Doped MoS2 Nanosheets Vertically Grown on Ti3C2 MXenes for Efficient Hydrodesulfurization in High-Temperature Environments. *ACS Appl. Nano Mater.* **2022**, *5* (7), 9666–9677 DOI: https://doi.org/10.1021/acsanm.2c01892.
11. Cao, H.; Bai, Z.; Li, Y.; Xiao, Z.; Zhang, X.; Li, G. Solvothermal Synthesis of Defect-Rich Mixed 1T-2H MoS2 Nanoflowers for Enhanced Hydrodesulfurization. *ACS Sustain. Chem. Eng.* **2020**, *8* (19), 7343–7352 DOI: https://doi.org/10.1021/acssuschemeng.0c00736.
12. Zhang, T.; Bai, Z.; Wang, L.; Zhang, X.; Li, G. Modulating Crystallization of MoS2 Nanostructures by Dimethyl Sulfoxide for Enhanced Hydrodesulfurization. *ACS Appl. Nano Mater.* **2023**, *6* (23), 21752–21762 DOI: https://doi.org/10.1021/acsanm.3c03951.

ISSN-e 2594-0317

13. Zheng, P.; Duan, A.; Chi, K.; Zhao, L.; Zhang, C.; Xu, C.; Zhao, Z.; Song, W.; Wang, X.; Fan, J. Influence of Sulfur Vacancy on Thiophene Hydrodesulfurization Mechanism at Different MoS2 Edges: A DFT Study. *Chem. Eng. Sci.* **2017**, *164*, 292–306 DOI: https://doi.org/10.1016/j.ces.2017.02.037.
14. Prodhomme, P.-Y.; Raybaud, P.; Toulhoat, H. Free-Energy Profiles along Reduction Pathways of MoS2 M-Edge and S-Edge by Dihydrogen: A First-Principles Study. *J. Catal.* **2011**, *280* (2), 178–195 DOI: https://doi.org/10.1016/j.jcat.2011.03.017.
15. Rosen, A. S.; Notestein, J. M.; Snurr, R. Q. Comprehensive Phase Diagrams of MoS2 Edge Sites Using Dispersion-Corrected DFT Free Energy Calculations. *J. Phys. Chem. C* **2018**, *122* (27), 15318–15329 DOI: https://doi.org/10.1021/acs.jpcc.8b02524.
16. Sharifvaghefi, S.; Yang, B.; Zheng, Y. New Insights on the Role of H2S and Sulfur Vacancies on Dibenzothiophene Hydrodesulfurization over MoS2 Edges. *Appl. Catal. Gen.* **2018**, *566*, 164–173 DOI: https://doi.org/10.1016/j.apcata.2018.05.033.
17. Mundotiya, S.; Singh, R.; Saha, S.; Kakkar, R.; Pal, S.; Kunzru, D.; Pala, R. G. S.; Sivakumar, S. Effect of Sodium on Ni-Promoted MoS2 Catalyst for Hydrodesulfurization Reaction: Combined Experimental and Simulation Study. *Energy Fuels* **2021**, *35* (3), 2368–2378 DOI: https://doi.org/10.1021/acs.energyfuels.0c02879.
18. Liu, Y.; Guan, S.; Du, X.; Chen, Y.; Yang, Y.; Chen, K.; Zheng, Z.; Wang, X.; Shen, X.; Hu, C.; Li, X. S-Vacancy Defect and Transition-Metal Atom Doping to Trigger Hydrogen Evolution of Two-Dimensional MoS2. *Energy Fuels* **2023**, *37* (7), 5370–5377 DOI: https://doi.org/10.1021/acs.energyfuels.2c03942.
19. Del Plá, J.; Bof, L. P.; Pis Diez, R. MoCo and MoWNi Clusters as Models for Hydrodesulfurization: A DFT Study of the Geometric, Electronic, and Magnetic Properties of MomCon ($3 \leq m + n \leq 8$) and MoxWyNiz ($3 \leq x + y + z \leq 8$) Clusters. *J. Phys. Chem. C* **2019**, *123* (1), 868–877 DOI: https://doi.org/10.1021/acs.jpcc.8b09773.
20. De Proft, F. Basic Functions. In *Conceptual Density Functional Theory*; Liu, S., Ed.; John Wiley & Sons, Ltd, 2022; pp 17–46 DOI: https://doi.org/10.1002/9783527829941.ch2.
21. Domingo, L. R.; Ríos-Gutiérrez, M.; Pérez, P. Applications of the Conceptual Density Functional Theory Indices to Organic Chemistry Reactivity. *Molecules* **2016**, *21* (6) DOI: https://doi.org/10.3390/molecules21060748.
22. Huck, L. A.; Leigh, W. J. Kinetic and Mechanistic Studies of the Reactions of Diarylgermylenes and Tetraaryldigermenes with Carbon Tetrachloride. *Can. J. Chem.* **2011**, *89* (2), 241–255 DOI: https://doi.org/10.1139/V10-128.
23. Domingo, L. R.; Sáez, J. A. Understanding the Mechanism of Polar Diels–Alder Reactions. *Org. Biomol. Chem.* **2009**, *7* (17), 3576–3583 DOI: https://doi.org/10.1039/B909611F.
24. Bagaria, P.; Roy, R. K. Correlation of Global Electrophilicity with the Activation Energy in Single-Step Concerted Reactions. *J. Phys. Chem. A* **2008**, *112* (1), 97–105 DOI: https://doi.org/10.1021/jp073357z.
25. Pérez, P.; Domingo, L. R.; José Aurell, M.; Contreras, R. Quantitative Characterization of the Global Electrophilicity Pattern of Some Reagents Involved in 1,3-Dipolar Cycloaddition Reactions. *Tetrahedron* **2003**, *59* (17), 3117–3125 DOI: https://doi.org/10.1016/S0040-4020(03)00374-0.
26. Yang, H.; Fairbridge, C.; Chen, J.; Ring, Z. Structure-HDS Reactivity Relationship of Dibenzothiophenes Based on Density Functional Theory. *Catal. Lett.* **2004**, *97* (3), 217–222 DOI: https://doi.org/10.1023/B:CATL.0000038587.25800.7e.
27. García-Cruz, I.; Valencia, D.; Klimova, T.; Oviedo-Roa, R.; Martínez-Magadán, J. M.; Gómez-Balderas, R.; Illas, F. Proton Affinity of S-Containing Aromatic Compounds: Implications for Crude Oil Hydrodesulfurization. *J. Mol. Catal. Chem.* **2008**, *281* (1), 79–84 DOI: https://doi.org/10.1016/j.molcata.2007.08.031.

ISSN-e 2594-0317

28. Li, H.; Zhu, W.; Zhu, S.; Xia, J.; Chang, Y.; Jiang, W.; Zhang, M.; Zhou, Y.; Li, H. The Selectivity for Sulfur Removal from Oils: An Insight from Conceptual Density Functional Theory. *AIChE J.* **2016**, *62* (6), 2087–2100 DOI: https://doi.org/10.1002/aic.15161.
29. Frisch, M. J.; Trucks, G. W.; Schlegel, H. B.; Scuseria, G. E.; Robb, M. A.; Cheeseman, J. R.; Scalmani, G.; Barone, V.; Petersson, G. A.; Nakatsuji, H.; Li, X.; Caricato, M.; Marenich, A. V.; Bloino, J.; Janesko, B. G.; Gomperts, R.; Mennucci, B.; Hratchian, H. P.; Ortiz, J. V.; Izmaylov, A. F.; Sonnenberg, J. L.; Williams-Young, D.; Ding, F.; Lipparini, F.; Egidi, F.; Goings, J.; Peng, B.; Petrone, A.; Henderson, T.; Ranasinghe, D.; Zakrzewski, V. G.; Gao, J.; Rega, N.; Zheng, G.; Liang, W.; Hada, M.; Ehara, M.; Toyota, K.; Fukuda, R.; Hasegawa, J.; Ishida, M.; Nakajima, T.; Honda, Y.; Kitao, O.; Nakai, H.; Vreven, T.; Throssell, K.; Montgomery Jr., J. A.; Peralta, J. E.; Ogliaro, F.; Bearpark, M. J.; Heyd, J. J.; Brothers, E. N.; Kudin, K. N.; Staroverov, V. N.; Keith, T. A.; Kobayashi, R.; Normand, J.; Raghavachari, K.; Rendell, A. P.; Burant, J. C.; Iyengar, S. S.; Tomasi, J.; Cossi, M.; Millam, J. M.; Klene, M.; Adamo, C.; Cammi, R.; Ochterski, J. W.; Martin, R. L.; Morokuma, K.; Farkas, O.; Foresman, J. B.; Fox, D. J. Gaussian 09, Revision D.01; Gaussian, Inc.: Wallingford, CT, 2013.
30. Perdew, J. P.; Burke, K.; Ernzerhof, M. Generalized Gradient Approximation Made Simple. *Phys. Rev. Lett.* **1996**, *77* (18), 3865–3868 DOI: https://doi.org/10.1103/PhysRevLett.77.3865.
31. Perdew, J. P.; Burke, K.; Ernzerhof, M. Errata: Generalized Gradient Approximation Made Simple. *Phys. Rev. Lett.* **1997**, *78* (7), 1396 DOI: https://doi.org/10.1103/PhysRevLett.78.1396.
32. Schäfer, A.; Huber, C.; Ahlrichs, R. Fully Optimized Contracted Gaussian Basis Sets of Triple Zeta Valence Quality for Atoms Li to Kr. *J. Chem. Phys.* **1994**, *100* (8), 5829–5835 DOI: https://doi.org/10.1063/1.467146.
33. Schäfer, A.; Horn, H.; Ahlrichs, R. Fully Optimized Contracted Gaussian Basis Sets for Atoms Li to Kr. *J. Chem. Phys.* **1992**, *97* (4), 2571–2577 DOI: https://doi.org/10.1063/1.463096.
34. Weigend, F. Accurate Coulomb-Fitting Basis Sets for H to Rn. *Phys. Chem. Chem. Phys.* **2006**, *8* (9), 1057–1065 DOI: https://doi.org/10.1039/B515623H.
35. Weigend, F.; Ahlrichs, R. Balanced Basis Sets of Split Valence, Triple Zeta Valence and Quadruple Zeta Valence Quality for H to Rn: Design and Assessment of Accuracy. *Phys. Chem. Chem. Phys.* **2005**, *7* (18), 3297–3305 DOI: https://doi.org/10.1039/B508541A.
36. Grimme, S.; Ehrlich, S.; Goerigk, L. Effect of the Damping Function in Dispersion Corrected Density Functional Theory. *J. Comput. Chem.* **2011**, *32* (7), 1456–1465 DOI: https://doi.org/10.1002/jcc.21759.
37. Ding, S.; Zhou, Y.; Wei, Q.; Jiang, S.; Zhou, W. Substituent Effects of 4,6-DMDBT on Direct Hydrodesulfurization Routes Catalyzed by Ni-Mo-S Active Nanocluster—A Theoretical Study. *Catal. Today* **2018**, *305*, 28–39 DOI: https://doi.org/10.1016/j.cattod.2017.10.040.
38. Wang, W.; Li, H.; Han, W.; Zhang, L.; Zhao, X.; Li, M. A DFT Study on the Adsorption Behavior of Sulfur and Nitrogen Compounds on the NiMoS Phase. *China Pet. Process. Petrochem. Technol.* **2020**, *22* (1), 40–48.
39. Liu, X.; Fan, X.; Wang, L.; Sun, J.; Wei, Q.; Zhou, Y.; Huang, W. Competitive Adsorption between Sulfur- and Nitrogen-Containing Compounds over NiMoS Nanocluster: The Correlations of Electronegativity, Morphology and Molecular Orbital with Adsorption Strength. *Chem. Eng. Sci.* **2021**, *231*, 116313 DOI: https://doi.org/10.1016/j.ces.2020.116313.
40. Sattayanon, C.; Namuangruk, S.; Kungwan, N.; Kunaseth, M. Reaction and Free-Energy Pathways of Hydrogen Activation on Partially Promoted Metal Edge of CoMoS and NiMoS: A DFT and Thermodynamics Study. *Fuel Process. Technol.* **2017**, *166*, 217–227 DOI: https://doi.org/10.1016/j.fuproc.2017.06.003.
41. Hirshfeld, F. L. Bonded-Atom Fragments for Describing Molecular Charge Densities. *Theor. Chim. Acta* **1977**, *44* (2), 129–138 DOI: https://doi.org/10.1007/BF00549096.

ISSN-e 2594-0317

42. Orita, H.; Uchida, K.; Itoh, N. Ab Initio Density Functional Study of the Structural and Electronic Properties of an MoS2 Catalyst Model: A Real Size Mo27S54 Cluster. *J. Mol. Catal. Chem.* **2003**, *195* (1), 173–180 DOI: https://doi.org/10.1016/S1381-1169(02)00528-9.
43. McQuarrie, D. A.; Simon, J. D. *Molecular Thermodynamics*; University Science Books: : Sausalito, CA, 1999.
44. Egorova, M.; Prins, R. Hydrodesulfurization of Dibenzothiophene and 4,6-Dimethyldibenzothiophene over Sulfided NiMo/γ-Al2O3, CoMo/γ-Al2O3, and Mo/γ-Al2O3 Catalysts. *J. Catal.* **2004**, *225* (2), 417–427 DOI: https://doi.org/10.1016/j.jcat.2004.05.002.
45. Bollinger, M. V.; Jacobsen, K. W.; Nørskov, J. K. Atomic and Electronic Structure of MoS2 Nanoparticles. *Phys. Rev. B* **2003**, *67* (8), 085410 DOI: https://doi.org/10.1103/PhysRevB.67.085410.
46. Raybaud, P. Understanding and Predicting Improved Sulfide Catalysts: Insights from First Principles Modeling. *Appl. Catal. Gen.* **2007**, *322*, 76–91 DOI: https://doi.org/10.1016/j.apcata.2007.01.005.
47. Dickinson, R. G.; Pauling, L. THE CRYSTAL STRUCTURE OF MOLYBDENITE. *J. Am. Chem. Soc.* **1923**, *45* (6), 1466–1471 DOI: https://doi.org/10.1021/ja01659a020.
48. Lauritsen, J. V.; Kibsgaard, J.; Helveg, S.; Topsøe, H.; Clausen, B. S.; Lægsgaard, E.; Besenbacher, F. Size-Dependent Structure of MoS2 Nanocrystals. *Nat. Nanotechnol.* **2007**, *2* (1), 53–58 DOI: https://doi.org/10.1038/nnano.2006.171.
49. Lauritsen, J. V.; Kibsgaard, J.; Olesen, G. H.; Moses, P. G.; Hinnemann, B.; Helveg, S.; Nørskov, J. K.; Clausen, B. S.; Topsøe, H.; Lægsgaard, E.; Besenbacher, F. Location and Coordination of Promoter Atoms in Co- and Ni-Promoted MoS2-Based Hydrotreating Catalysts. *J. Catal.* **2007**, *249* (2), 220–233 DOI: https://doi.org/10.1016/j.jcat.2007.04.013.
50. Rangarajan, S.; Mavrikakis, M. DFT Insights into the Competitive Adsorption of Sulfur- and Nitrogen-Containing Compounds and Hydrocarbons on Co-Promoted Molybdenum Sulfide Catalysts. *ACS Catal.* **2016**, *6* (5), 2904–2917 DOI: https://doi.org/10.1021/acscatal.6b00058.
51. Šarić, M.; Rossmeisl, J.; Moses, P. G. Modeling the Adsorption of Sulfur Containing Molecules and Their Hydrodesulfurization Intermediates on the Co-Promoted MoS2 Catalyst by DFT. *J. Catal.* **2018**, *358*, 131–140 DOI: https://doi.org/10.1016/j.jcat.2017.12.001.
52. Ataca, C.; Şahin, H.; Ciraci, S. Stable, Single-Layer MX2 Transition-Metal Oxides and Dichalcogenides in a Honeycomb-Like Structure. *J. Phys. Chem. C* **2012**, *116* (16), 8983–8999 DOI: https://doi.org/10.1021/jp212558p.
53. Kuchitsu, K. *Landolt-Bornstein: Group II: Atomic and Molecular Physics Volume 15: Structure Data of Free Polyatomic Molecules*; Kuchitsu, K., Ed.; Springer-Verlag: Berlin, Heidelberg, 1987; Vol. 15 DOI: https://doi.org/10.1007/978-3-642-45748-7_1.
54. Moses, P. G.; Grabow, L. C.; Fernandez Sanchez, E.; Hinnemann, B.; Topsøe, H.; Knudsen, K. G.; Norskov, J. K. Trends in Hydrodesulfurization Catalysis Based on Realistic Surface Models. *Catal. Lett.* **2014**, *144* (8), 1425–1432 DOI: https://doi.org/10.1007/s10562-014-1279-4.
55. Kaddouri, Y.; Abrigach, F.; Yousfi, E. B.; Kodadi, M. E. New Thiazole, Pyridine and Pyrazole Derivatives as Antioxidant Candidates: Synthesis, DFT Calculations and Molecular Docking Study. *Heliyon* **2020**, *6* (1), 1–9 DOI: https://doi.org/j.heliyon.2020.e03185.
56. Tuxen, A. K.; Füchtbauer, H. G.; Temel, B.; Hinnemann, B.; Topsøe, H.; Knudsen, K. G.; Besenbacher, F.; Lauritsen, J. V. Atomic-Scale Insight into Adsorption of Sterically Hindered Dibenzothiophenes on MoS2 and Co–Mo–S Hydrotreating Catalysts. *J. Catal.* **2012**, *295*, 146–154 DOI: https://doi.org/10.1016/j.jcat.2012.08.004.